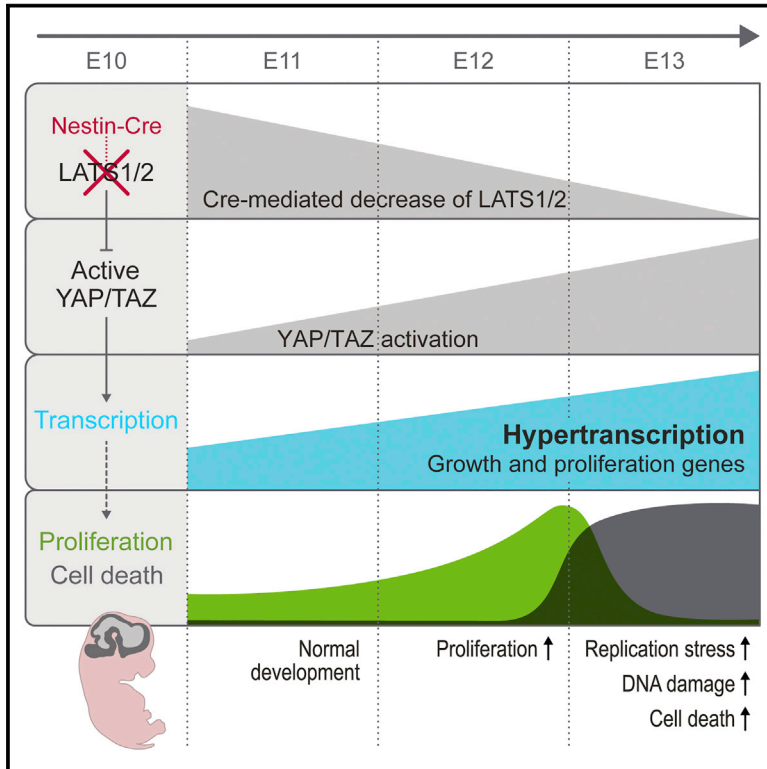


# Developmental Cell

## The Hippo Pathway Prevents YAP/TAZ-Driven Hypertranscription and Controls Neural Progenitor Number

### Graphical Abstract



### Authors

Alfonso Lavado, Jun Young Park, Joshua Paré, ..., Peter J. McKinnon, Randy L. Johnson, Xinwei Cao

### Correspondence

xinwei.cao@stjude.org

### In Brief

Using cell-number-normalized transcriptome analysis, Lavado et al. show that inactivation of Hippo pathway LATS1/2 kinases during brain development causes YAP/TAZ-driven global hypertranscription, upregulating many genes involved in cell growth and proliferation. Hypertranscription in neural progenitors inhibits differentiation and triggers replication stress and DNA damage, resulting in massive apoptosis.

### Highlights

- Loss of Hippo pathway LATS kinase leads to YAP/TAZ-driven global hypertranscription
- YAP/TAZ-driven hypertranscription upregulates many growth and proliferation genes
- Hypertranscription impairs neural progenitor differentiation and causes apoptosis
- Cell-number-normalized methods are required to detect global hypertranscription

# The Hippo Pathway Prevents YAP/TAZ-Driven Hypertranscription and Controls Neural Progenitor Number

Alfonso Lavado,<sup>1</sup> Jun Young Park,<sup>1</sup> Joshua Paré,<sup>1</sup> David Finkelstein,<sup>2</sup> Haitao Pan,<sup>3</sup> Beisi Xu,<sup>2</sup> Yiping Fan,<sup>2</sup> Ram Parikshan Kumar,<sup>1</sup> Geoffrey Neale,<sup>4</sup> Young Don Kwak,<sup>5</sup> Peter J. McKinnon,<sup>5</sup> Randy L. Johnson,<sup>6</sup> and Xinwei Cao<sup>1,7,\*</sup>

<sup>1</sup>Department of Developmental Neurobiology, St. Jude Children's Research Hospital, Memphis, TN 38105, USA

<sup>2</sup>Department of Computational Biology, St. Jude Children's Research Hospital, Memphis, TN 38105, USA

<sup>3</sup>Department of Biostatistics, St. Jude Children's Research Hospital, Memphis, TN 38105, USA

<sup>4</sup>Hartwell Center for Bioinformatics and Biotechnology, St. Jude Children's Research Hospital, Memphis, TN 38105, USA

<sup>5</sup>Department of Genetics, St. Jude Children's Research Hospital, Memphis, TN 38105, USA

<sup>6</sup>Department of Cancer Biology, University of Texas MD Anderson Cancer Center, Houston, TX 77030, USA

<sup>7</sup>Lead Contact

\*Correspondence: [xinwei.cao@stjude.org](mailto:xinwei.cao@stjude.org)

<https://doi.org/10.1016/j.devcel.2018.09.021>

## SUMMARY

The Hippo pathway controls the activity of YAP/TAZ transcriptional coactivators through a kinase cascade. Despite the critical role of this pathway in tissue growth and tumorigenesis, it remains unclear how YAP/TAZ-mediated transcription drives proliferation. By analyzing the effects of inactivating LATS1/2 kinases, the direct upstream inhibitors of YAP/TAZ, on mouse brain development and applying cell-number-normalized transcriptome analyses, we discovered that YAP/TAZ activation causes a global increase in transcription activity, known as hypertranscription, and upregulates many genes associated with cell growth and proliferation. In contrast, conventional read-depth-normalized RNA-sequencing analysis failed to detect the scope of the transcriptome shift and missed most relevant gene ontologies. Following a transient increase in proliferation, however, hypertranscription in neural progenitors triggers replication stress, DNA damage, and p53 activation, resulting in massive apoptosis. Our findings reveal a significant impact of YAP/TAZ activation on global transcription activity and have important implications for understanding YAP/TAZ function.

## INTRODUCTION

The Hippo pathway regulates the development, homeostasis, regeneration, and tumorigenesis of various tissues across species (Pfleger, 2017; Yu et al., 2015). At its core are a kinase cascade and a transcription factor (TF) complex (Meng et al., 2016). The upstream kinases MST1 and MST2 activate the downstream kinases LATS1 and LATS2 (LATS1/2), which in turn phosphorylate the homologous transcriptional coactivators YAP and TAZ (YAP/TAZ)—the key effectors of the Hippo

pathway—resulting in their cytoplasmic sequestration or degradation. When the Hippo kinase cascade is inactivated, unphosphorylated YAP/TAZ enter the nucleus, where they interact with the TEAD family of DNA-binding factors and activate gene expression. The most prominent function of YAP/TAZ is to promote cell proliferation and survival. Accordingly, animal models of Hippo pathway inactivation or YAP/TAZ activation almost always exhibit overgrowth or tumorigenic phenotypes, and YAP/TAZ activation has been observed in nearly all types of human solid tumor and is associated with tumor aggression and poor outcomes (Zanconato et al., 2016). Despite this, the genes that are consistently and strongly induced by YAP/TAZ in different contexts are often those related to the extracellular matrix (ECM), cell adhesion, and epithelial-to-mesenchymal transition (EMT) and are rarely those related to proliferation (Cai et al., 2015; Lavado et al., 2013; Lee et al., 2016; Ota and Sasaki, 2008; Su et al., 2015), raising the question of how YAP/TAZ activation drives proliferation in so many contexts.

As LATS1/2 directly phosphorylate YAP/TAZ, they are probably the most important gatekeepers of YAP/TAZ activation in many contexts. Indeed, mice lacking *Lats1/2* in the developing gut (Cotton et al., 2017), kidney (Reginensi et al., 2016), and liver (Lee et al., 2016); in growing blood vessels (Kim et al., 2017); and in the adult liver (Chen et al., 2015; Lee et al., 2016) and heart (Heallen et al., 2013) all show YAP/TAZ activation. This in turn promotes the proliferation of gut mesenchymal progenitors, immature liver biliary epithelial cells, vascular endothelial cells, and adult cardiomyocytes in the corresponding tissues and organs. Surprisingly, in the adult mouse liver, YAP/TAZ activation induced by *Lats1/2* deletion triggered hepatocyte senescence and death (Lee et al., 2016). Although polyploidy and markers of DNA damage and p53 activation were detected, the cause of these defects was unclear.

In the developing mammalian brain, apical neural progenitor cells (NPCs), including neuroepithelial cells and radial glial cells (RGCs), form an epithelial layer along the ventricles—a region known as the ventricular zone (VZ) (Kriegstein and Alvarez-Buylla, 2009). An RGC can undergo proliferative division to expand itself or neurogenic division to generate a new RGC

and either a neuron or an intermediate progenitor cell (IPC). IPCs, residing in the subventricular zone (SVZ), produce more neurons through rounds of neurogenic division. Newborn neurons migrate outward through the intermediate zone (IZ) and settle at appropriate locations in the cortical plate (CP) to complete their differentiation. Precise orchestration of NPC proliferation, differentiation, and survival is critical for generating a brain with diverse types and the correct numbers of cells.

We investigated the role of LATS1/2 in mouse brain development. We found that the loss of *Lats1/2* in apical NPCs results in their transient expansion, quickly followed by massive apoptosis, reduced differentiation, and tissue disintegration. These defects result from YAP/TAZ activation, as additional *Yap;Taz* deletion restores brain development. By applying cell-number-normalized (CNN) transcriptome analysis, we discovered that YAP/TAZ activation boosts global transcription activity and upregulates many genes associated with increased biosynthetic capacity and proliferation. In contrast, conventional RNA-sequencing (RNA-seq) analysis failed to detect the scope of the transcriptome shift and missed most relevant gene ontologies. Furthermore, this global transcription increase in NPCs causes DNA replication stress and DNA damage and triggers apoptosis. Our study reveals a mechanism by which YAP/TAZ-mediated transcription drives proliferation and highlights cell type-specific responses to YAP/TAZ activation.

## RESULTS

### ***Lats1/2* Deletion Activates YAP/TAZ, Expands RGCs, and Triggers Massive Apoptosis**

To determine the role of LATS1/2 during mammalian brain development, we generated *Lats1/2* conditional knockout (KO) mice by using *Nestin-Cre*, which is expressed in apical NPCs starting on embryonic day (E) 10.5 (Tronche et al., 1999). Brains of single KO mice or those lacking three *Lats* alleles developed normally (Figure S1D and data not shown), whereas double KO (dKO, *Lats1/2<sup>fl/fl</sup>;Nestin-Cre*) brains exhibited severe phenotypes and were the focus of this study. Compared to the levels in control (no *Cre*) brains, phospho-YAP levels gradually decreased and YAP/TAZ levels gradually increased in E12.5 and E13.5 dKO brains (Figure 1A), consistent with the established Hippo kinase cascade. In control E12.5 brains, YAP/TAZ were specifically expressed in Sox2+ RGCs (Bylund et al., 2003) and were largely cytoplasmic (Figure 1B). In *Lats1/2* dKO brains, large portions of YAP/TAZ proteins shifted to the nucleus. Subcellular fractionation further confirmed a significant nuclear enrichment of YAP/TAZ proteins in dKO brains (Figure S1A). Thus, *Lats1/2* deletion results in the upregulation of YAP/TAZ proteins and their nuclear translocation.

Next, we examined the effect of *Lats1/2* deletion on cortical RGC proliferation and differentiation. At E12.5, the numbers of Sox2+Tbr2– RGCs, Tbr2+ IPCs (Englund et al., 2005), and P27+ neurons (Nguyen et al., 2006) per 500- $\mu$ m cortex length were unchanged in dKO brains (Figure S1B). However, the area of cortical VZ demarcated by Pax6 immunosignal (Englund et al., 2005) was increased in the rostral region of dKO brains (Figures 1C and S1C), suggesting lateral expansion of the RGC population. We then measured RGC cell-cycle length by a cumulative EdU/BrdU-labeling paradigm (Pilaz et al., 2016).

Both the S-phase ( $T_s$ ) and total cell-cycle ( $T_c$ ) lengths of dKO RGCs were shortened (Figure 1D). Thus, *Lats1/2* deletion accelerates the cell cycle of E12.5 cortical RGCs, leading to their expansion.

The morphology of *Lats1/2* dKO brains deteriorated quickly. At E13.5, there was obvious disruption of the neuroepithelial structure and ventricular enlargement (Figure 1E). At E15.5, the rostral region had disintegrated into a disorganized mass of cells, and only a thin layer of cells was left in the rest of the brain (Figure 1E). Such severe dysplasia prompted us to examine whether cell death was increased in dKO brains. Cleaved caspase-3 immunostaining revealed massive apoptosis in E13.5 dKO brains, especially at the border between the VZ/SVZ and the Tuj1+ CP (Figure 1F). RGCs were increased and IPCs decreased in E13.5 dKO cortices (Figure 1G), suggesting that *Lats1/2* deletion expands RGCs and impairs their differentiation into IPCs, although IPC reduction may be secondary to apoptosis.

### **Apoptosis in LATS-Deficient Brains Depends on p53 Activation**

To uncover the cause of LATS-deficiency phenotypes, we used Affymetrix microarrays to compare the transcriptomes of E12.5 control and dKO cortices before the onset of apoptosis and tissue dysplasia (Figure S2A) and found upregulation of the “p53 signaling pathway” by gene set enrichment analysis (Table S1 and Figure S2B). Immunostaining confirmed an increase in p53 proteins in E13.5, but not E12.5, dKO brains (Figures 2A and S2A) probably because microarrays are more sensitive than immunostaining. Because p53 is stabilized in response to various cellular stresses, including DNA damage (Mello and Attardi, 2018), we stained brain sections for the DNA damage markers  $\gamma$ H2AX (Rogakou et al., 2000; Rogakou et al., 1998) and phospho-KAP1 (White et al., 2006; Ziv et al., 2006). Both markers revealed widespread DNA damage in E13.5 dKO brains (Figure 2A).

To determine whether the apoptosis in *Lats1/2* dKO brains depended on p53, we generated *Lats1/2;p53* triple KO (tKO) mice with *Emx1-Cre*, which drives cortex-specific deletion starting on E9.5 (Gorski et al., 2002). Mice carrying *Emx1-Cre* can be maintained as homozygous, increasing the chance of producing tKO mice. Deleting *Lats1/2* with *Emx1-cre* also led to massive apoptosis (Figure 2B); this was similar to the result with *Nestin-Cre* but occurred earlier (at E12.5) because *Emx1-Cre* is turned on before *Nestin-Cre*. The additional removal of *p53* greatly diminished apoptosis (Figure 2B).  $\gamma$ H2AX was even more elevated in tKO cortex than in *Lats1/2* dKO cortex (Figure 2B), indicative of aberrant survival of DNA-damaged cells in the absence of p53. These data suggest that apoptosis in *Lats1/2* dKO brains is largely p53 dependent and that DNA damage is upstream or independent of p53 activation.

Despite apoptosis being prevented, *Lats1/2;p53* tKO cortex was far from normal. At E12.5, both dKO and tKO cortices showed structural disorganization, apical junction disruption, and depletion of Tbr2+ IPCs (Figures 2B and S2C). At E15.5, both dKO and tKO cortices completely lacked layering organization and contained markedly fewer Satb2+ and Tbr1+ neurons than control cortex (Figure 2C). In summary, the loss of *Lats1/2* in NPCs triggers widespread DNA damage and p53-dependent apoptosis. It also causes severe disorganization of

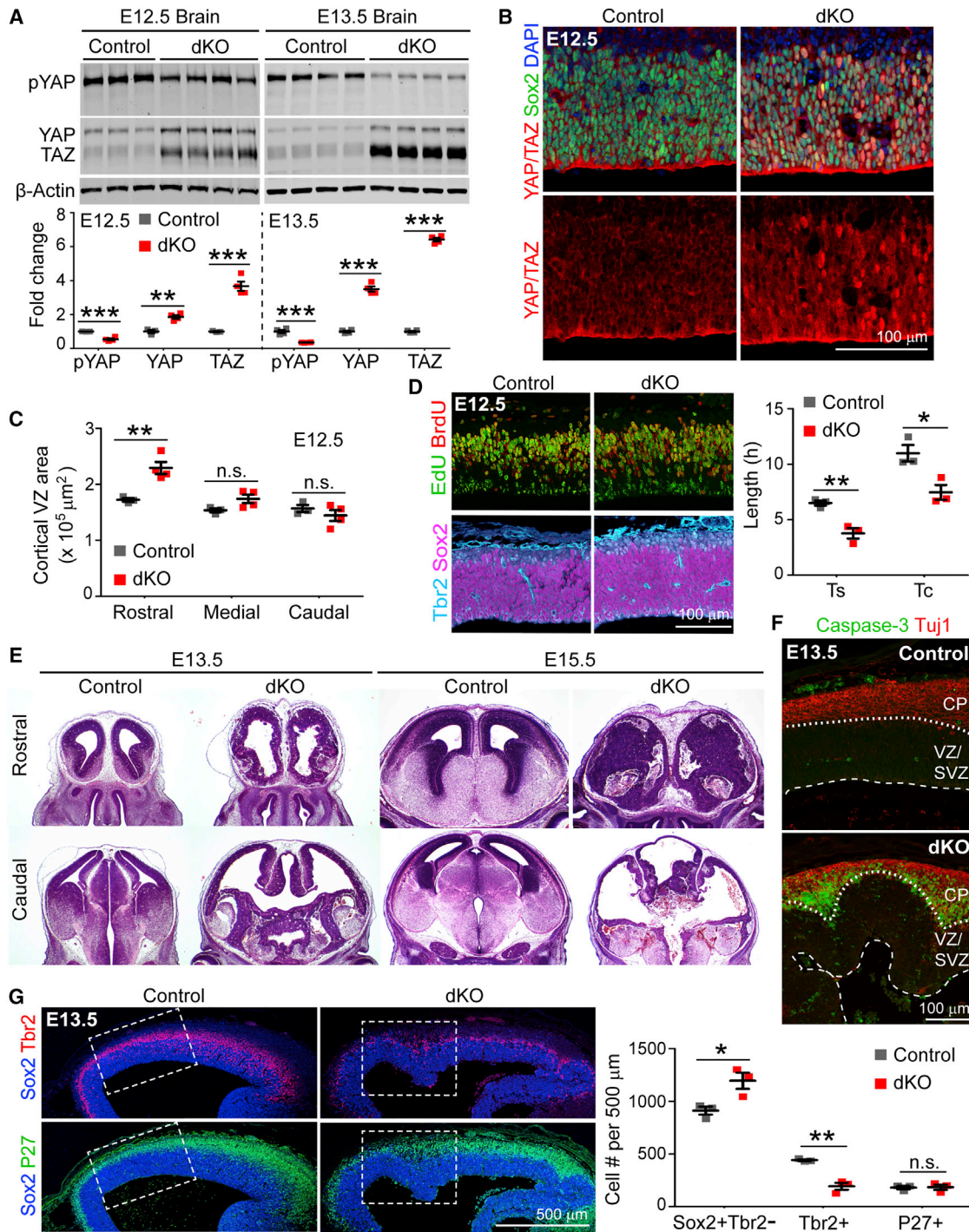


**Figure 1. *Lats1/2* Deletion Activates YAP/TAZ, Expands RGCs, and Triggers Massive Apoptosis.**

(A) Quantitative western blots comparing protein levels in control (no Cre) and *Lats1/2* dKO (*Lats1/2*<sup>F/F</sup>; *Nestin-Cre*) brains.

(B) Immunostaining showing YAP/TAZ localization in E12.5 cortices.

(C) Quantification of E12.5 cortical ventricular zone (VZ) area based on Pax6 immunostaining.

(D) Immunostaining and quantification of the S-phase length (Ts) and total cell-cycle length (Tc) of E12.5 Sox2+Tbr2<sup>-</sup> RGCs by cumulative EdU/BrdU labeling.

(E) H&E staining showing gross morphologic defects in dKO brains.

(F) Immunostaining for cleaved caspase-3 to detect apoptosis in E13.5 cortices. Dashed lines demarcate the ventricular surface; dotted lines mark the border between the ventricular/subventricular zone (VZ/SVZ) and the cortical plate (CP).

(G) Immunostaining and quantification of Sox2+Tbr2<sup>-</sup> RGCs, Tbr2<sup>+</sup> IPCs, and P27<sup>+</sup> neurons in E13.5 cortices. Dashed boxes indicate regions quantified.

Data are shown as mean ± SEM; \*p < 0.05; \*\*p < 0.01; \*\*\*p < 0.001; n.s., not significant; unpaired two-tailed Student's t test. See also Figure S1.

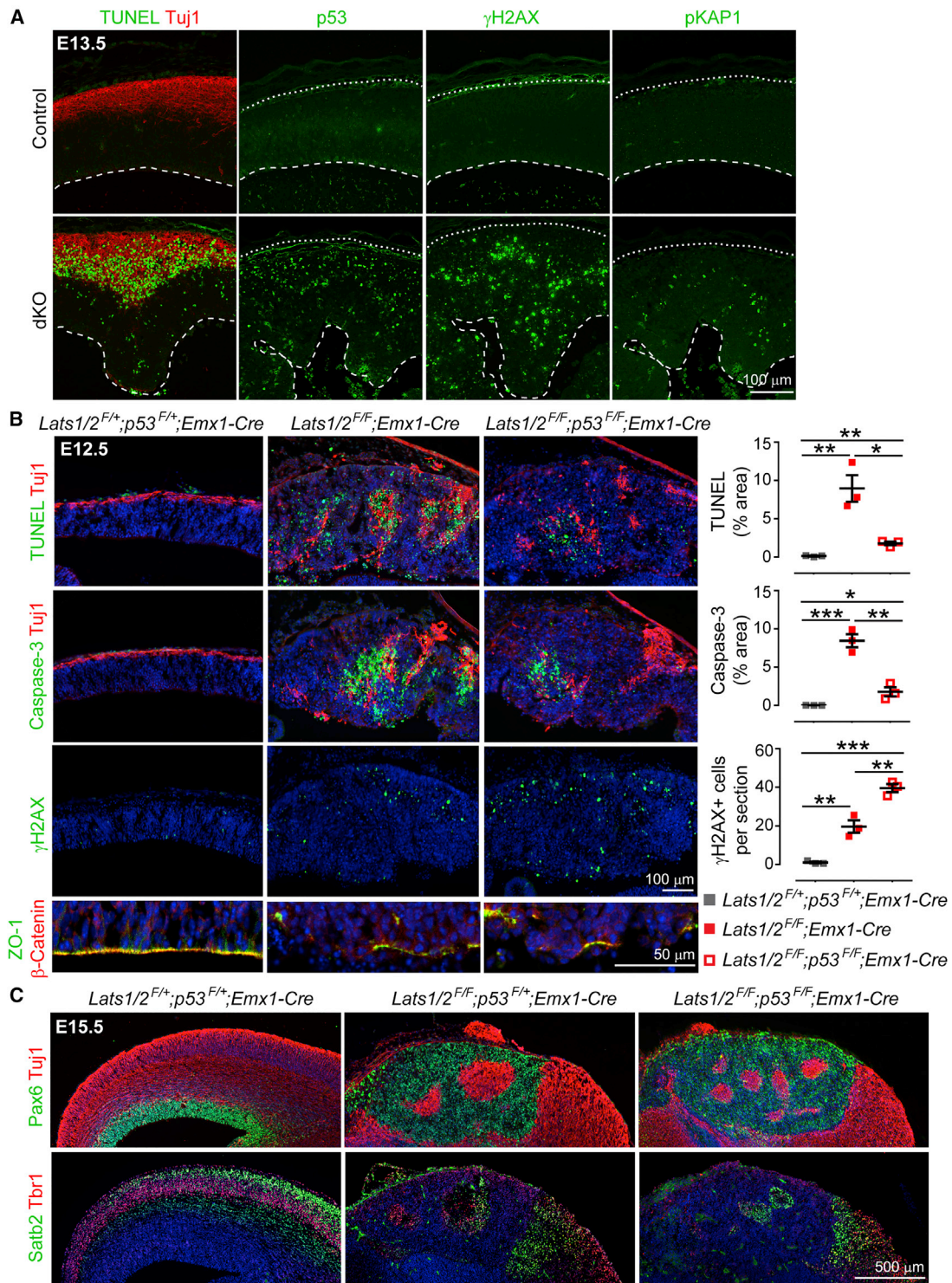


**Figure 2. Apoptosis in LATS-Deficient Brains Depends on p53 Activation**

(A) Images of TUNEL assay and immunostaining for DNA damage markers in E13.5 control and *Lats1/2;Nestin-Cre* dKO brains. Dashed lines demarcate the ventricular surface; solid lines demarcate the outer edge of the cortical plate.

(B) TUNEL assay, immunostaining, and quantification showing the effects of deleting *p53* in the *Lats1/2;Emx1-Cre* dKO background (mean  $\pm$  SEM). ZO-1 and  $\beta$ -catenin label apical junctions. \* $p < 0.05$ ; \*\* $p < 0.01$ ; \*\*\* $p < 0.001$ .

(C) Immunostaining for the RGC marker Pax6, the pan-neuronal marker Tuj1, and the layer-specific neuronal markers Satb2 and Tbr1, showing defects in E15.5 *Lats1/2;p53* KO brains.

The blue color in (B) and (C) is DAPI signal. See also [Figure S2](#) and [Table S1](#).

brain structures and impairs differentiation, independent of p53-induced apoptosis.

### Dysplasia of LATS-Deficient Brains Results from YAP/TAZ Activation

The apoptosis and dysplasia phenotypes of *Lats1/2* dKO brains were unexpected because Hippo kinase cascade inactivation and subsequent YAP/TAZ activation typically lead to tissue overgrowth. To test whether these phenotypes were due to YAP/TAZ activation, we deleted *Yap* and *Taz* in the *Lats1/2;Emx1-Cre* dKO background. At post-natal day 0 (P0), *Lats1/2* dKO cortex was markedly smaller than control cortex and was completely disorganized, with Pax6+ RGCs being misplaced outside the VZ, cortical neurons lacking layering organization, and their axons being severely reduced and unable to form normal projections (Figures 3A and S3A). Deleting *Yap* largely restored the size of the cortex, but its organization was notably defective, with numerous patches of RGCs intermingled with neurons throughout the CP (Figures 3A and S3A). Removing a further *Taz* allele largely restored the layering of cortical neurons, although some RGCs were still dispersed outside the VZ, and the corpus callosum (the axon tract connecting the cortical hemispheres) was still missing (Figures 3A and S3A). Completely removing *Yap* and *Taz* essentially restored cortex morphology (Figures 3A and S3A). These results indicate that YAP/TAZ activation is required for the dysplasia of LATS-deficient brains. The near-complete restoration of brain morphology by *Yap;Taz* deletion is in stark contrast to the severe disorganization and impaired differentiation of *Lats1/2;p53* tKO cortex, suggesting that YAP/TAZ activation mediates most, if not all, of the effects subsequent to *Lats1/2* loss, whereas p53 activation accounts for apoptosis induction only.

We further quantified apoptosis and RGC numbers upon additional *Yap;Taz* deletion (Figures 3B and 3C). Apoptosis was strongly elevated in E13.5 *Lats1/2* dKO cortex as compared to control cortex. Although apoptosis remained highly elevated after the additional deletion of one allele of *Yap*, it was reduced when both *Yap* alleles were deleted and returned to basal levels when three or four *Yap;Taz* alleles were deleted. The changes in RGC numbers exhibited developmental dynamics. At E13.5, RGCs were severely depleted in dKO cortex. They were restored to the numbers seen in controls when one *Yap* allele was deleted, increased further when both *Yap* alleles were deleted, and returned to the control numbers when three or four *Yap;Taz* alleles were deleted. At P0, dKO and control cortices contained similar numbers of RGCs, which were strongly expanded when one or two *Yap* alleles were deleted, expanded to a lesser degree when three *Yap;Taz* alleles were deleted, and decreased when all four alleles were deleted. These data revealed a clear dosage effect of *Yap;Taz* allele numbers, suggesting that the consequences of LATS inactivation depend on the levels of active YAP/TAZ: very high levels of active YAP/TAZ trigger massive apoptosis and severely deplete RGCs, whereas high-to-moderate levels of active YAP/TAZ expand RGCs and moderately elevate apoptosis.

To test whether YAP/TAZ activation was sufficient to induce apoptosis and block differentiation, we overexpressed YAP and its variants in the developing cortex by *in utero* electroporation. Although wild-type (WT) YAP did not induce cell death,

YAP<sup>5SA</sup>, which harbors mutations in 5 LATS phosphorylation sites and is thus resistant to LATS-mediated inhibition (Zhao et al., 2007), triggered significant cell death (Figure S3B). The YAP<sup>5SA/S94A</sup> mutant, which cannot bind TEAD (Zhao et al., 2007), failed to induce cell death, suggesting that the ability of YAP<sup>5SA</sup> to induce cell death depends on TEAD binding and probably on TEAD-mediated transcription. Consistent with our previous report (Cao et al., 2008), YAP overexpression maintained the RGC state and inhibited differentiation, as indicated by a larger fraction of transfected cells residing in the VZ/SVZ, a smaller fraction in the CP, and the presence of fewer Tbr2+ IPCs when compared to the results of control GFP transfections (Figures S3B and S3C). YAP<sup>5SA</sup> had even stronger effects: essentially all transfected cells remained as RGCs in the VZ, and few differentiated into IPCs (Figures S3B and S3C), which resembled the phenotypes of *Lats1/2* dKO brains (Figure 1G). Compared to control transfections, the YAP<sup>5SA/S94A</sup> mutant did not alter the fraction of cells in the VZ/SVZ or the number of IPCs, but it did cause retention of transfected cells in the IZ (Figures S3B and S3C); whether this reflects a normal function of YAP is unclear. These data indicate that ectopic, high levels of YAP/TAZ activation are sufficient to induce apoptosis and block differentiation and that TEAD-mediated transcription is probably required for this process.

### LATS-Deficient Neural Stem Cells in Culture Recapitulate *In Vivo* Phenotypes

Next, we employed neural stem cell (NSC) cultures in more mechanistic studies. We derived NSCs from E13.5 control and *Lats1/2;Nestin-Cre* dKO cortices. In adherent cultures, YAP/TAZ predominantly resided in the cytoplasm of control NSCs but showed strong nuclear localization in dKO NSCs (Figure 4A). p53 was detected at the background level in control cells but showed intense nuclear signals in dKO cells (Figure 4A). When grown in differentiation medium, dKO cells failed to undergo neuronal differentiation (Figure 4B), which resembled the differentiation defect observed *in vivo*. When grown as neurospheres, dKO spheres were smaller than control spheres and showed higher levels of cleaved caspase-3 immunosignal (Figures 4C and S4A). If all visible cell clusters were included, the numbers of neurospheres formed by control and dKO NSCs were similar; however, the viability and number of live cells were significantly lower in dKO cultures (Figure 4C), recapitulating the *in vivo* phenotype of increased apoptosis. NSCs derived from E12.5 dKO cortices exhibited similar defects (Figure S4B), indicating that phenotypically, they progressed in culture as they did *in vivo*.

We then tested whether the phenotypes exhibited by *Lats1/2* dKO NSCs in culture were mediated by p53 and YAP/TAZ. We transfected NSCs derived from *Lats1/2<sup>F/F</sup>*, *Lats1/2<sup>F/F</sup>;p53<sup>F/F</sup>*, and *Lats1/2<sup>F/F</sup>;Yap<sup>F/F</sup>;Taz<sup>F/F</sup>* cortices with plasmids encoding mCherry (control) or Cre-mCherry (Cre), then sorted mCherry+ cells and grew them in neurosphere cultures (Figure 4D). Like NSCs derived from *Lats1/2* dKO cortices, *Lats1/2<sup>F/F</sup>* cells transfected with Cre showed p53 upregulation and reduced viability and cell numbers when compared to control-transfected cells (Figures 4E and 4F). *Lats1/2<sup>F/F</sup>;p53<sup>F/F</sup>* and *Lats1/2<sup>F/F</sup>;Yap<sup>F/F</sup>;Taz<sup>F/F</sup>* cells transfected with Cre no longer exhibited p53 activation or less viability than the corresponding controls. Interestingly, whereas the cell number was restored in Cre-transfected

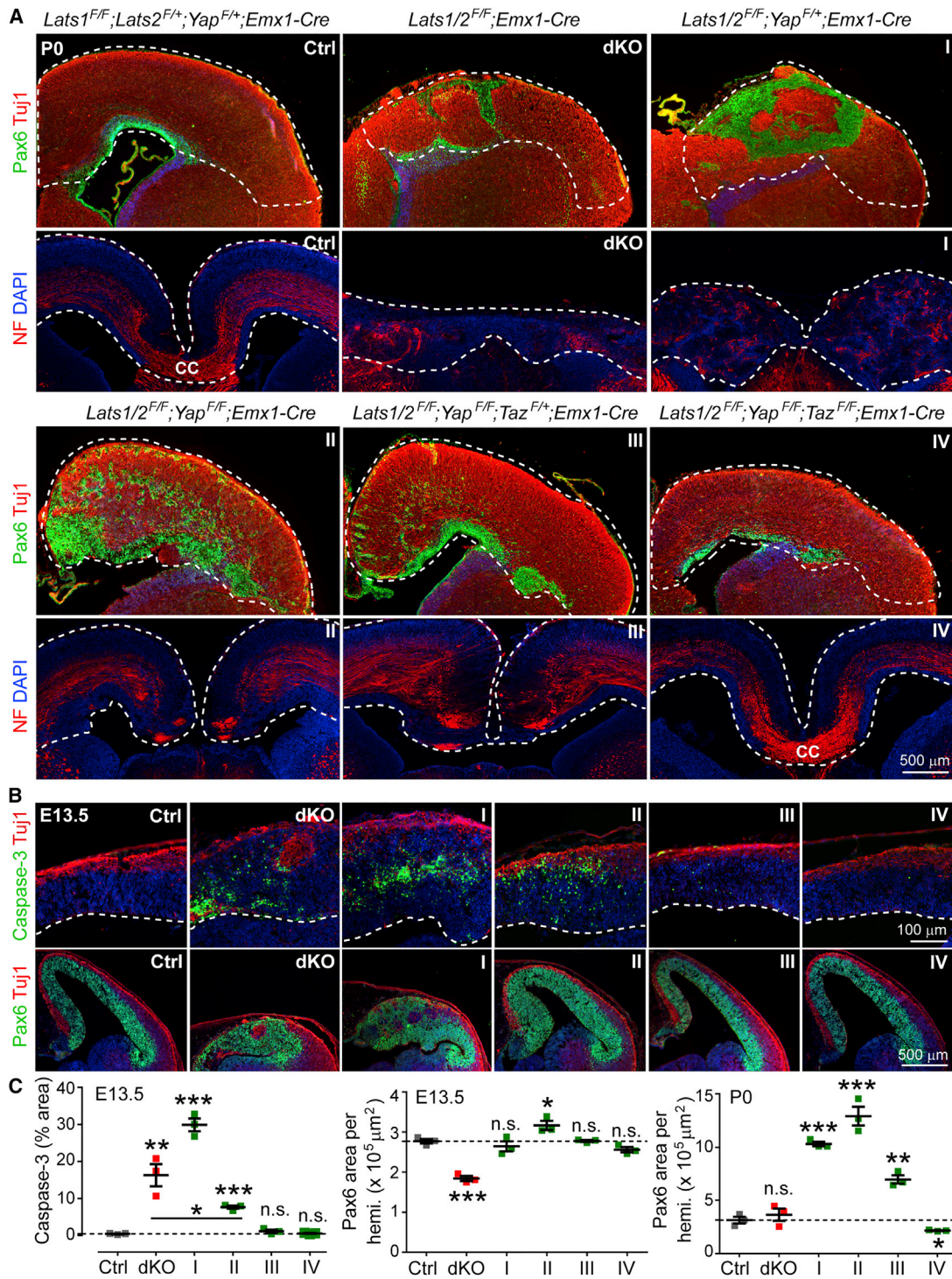


**Figure 3. Dysplasia of LATS-Deficient Brains Results from YAP/TAZ Activation**

(A) Pax6 and Tuj1 immunostaining images of one hemisphere and neurofilament (NF) immunostaining images of the midline region of P0 cortices, showing the effects of deleting *Yap* and *Taz* in the *Lats1/2* dKO background. Roman numerals indicate the number of *Yap*/*Taz* alleles deleted; Ctrl, control. The same naming scheme is used in (B) and (C). Dashed lines outline the cortex. CC, corpus callosum.

(B) Immunostaining of E13.5 brains showing the effects of deleting *Yap* and *Taz* in the *Lats1/2* dKO background. Dashed lines demarcate the ventricular surface. The blue color is DAPI signal.

(C) Quantification of E13.5 cleaved caspase-3 signals and E13.5 and P0 Pax6 signals (mean  $\pm$  SEM). Dashed lines indicate the mean values of control (Ctrl) samples. Comparisons are against the results with controls unless otherwise indicated. \*p < 0.05; \*\*p < 0.01; \*\*\*p < 0.001; n.s., not significant.

See also Figure S3.

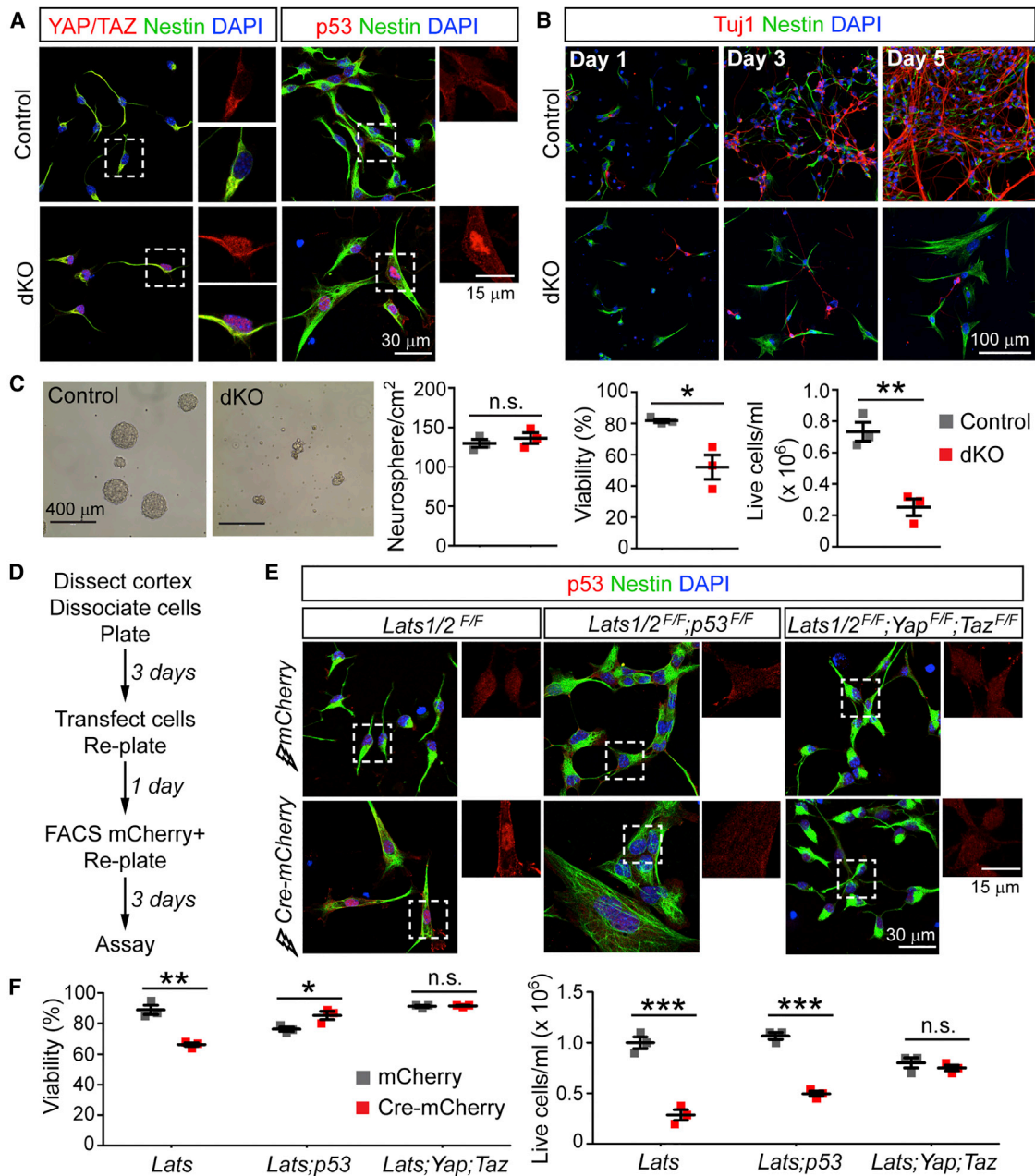


**Figure 4. LATS-Deficient Neural Stem Cells in Culture Recapitulate *In Vivo* Phenotypes**

(A) Immunostaining of NSCs in adherent cultures comparing YAP/TAZ localization and p53 levels in control and *Lats1/2;Nestin-Cre* dKO cells.

(B) Immunostaining of NSCs grown in differentiation medium for the neuronal marker Tuj1 and the progenitor marker nestin.

(C) Representative images and quantification of neurospheres 3 days after plating (mean ± SEM).

(D) Procedure for NSC transfection, sorting, and assay.

(E) Immunostaining showing p53 levels in cells of the indicated genotypes transfected with mCherry or Cre-mCherry plasmid.

(F) Quantification of NSCs with the indicated floxed alleles transfected with mCherry or Cre-mCherry plasmid 3 days after plating in neurosphere culture (mean ± SEM).

Dashed boxes in (A) and (E) indicate enlarged regions. \**p* < 0.05; \*\**p* < 0.01; \*\*\**p* < 0.001; n.s., not significant. See also Figure S4.

*Lats1/2<sup>F/F</sup>;Yap<sup>F/F</sup>;Taz<sup>F/F</sup>* cells, it was still significantly reduced in Cre-transfected *Lats1/2<sup>F/F</sup>;p53<sup>F/F</sup>* cells (Figure 4F), suggesting that the latter still had a proliferation defect. These results demonstrate that LATS-deficient NSCs in culture recapitulate many aspects of *Lats1/2* dKO phenotypes *in vivo*.

Although LATS1/2 have been implicated in mitosis (Hergovich and Hemmings, 2012), *Lats1/2* dKO NSCs showed very low levels of mitosis defects (Figures S4C–S4E) that are unlikely to account for the severe viability and proliferation defects of these cells.

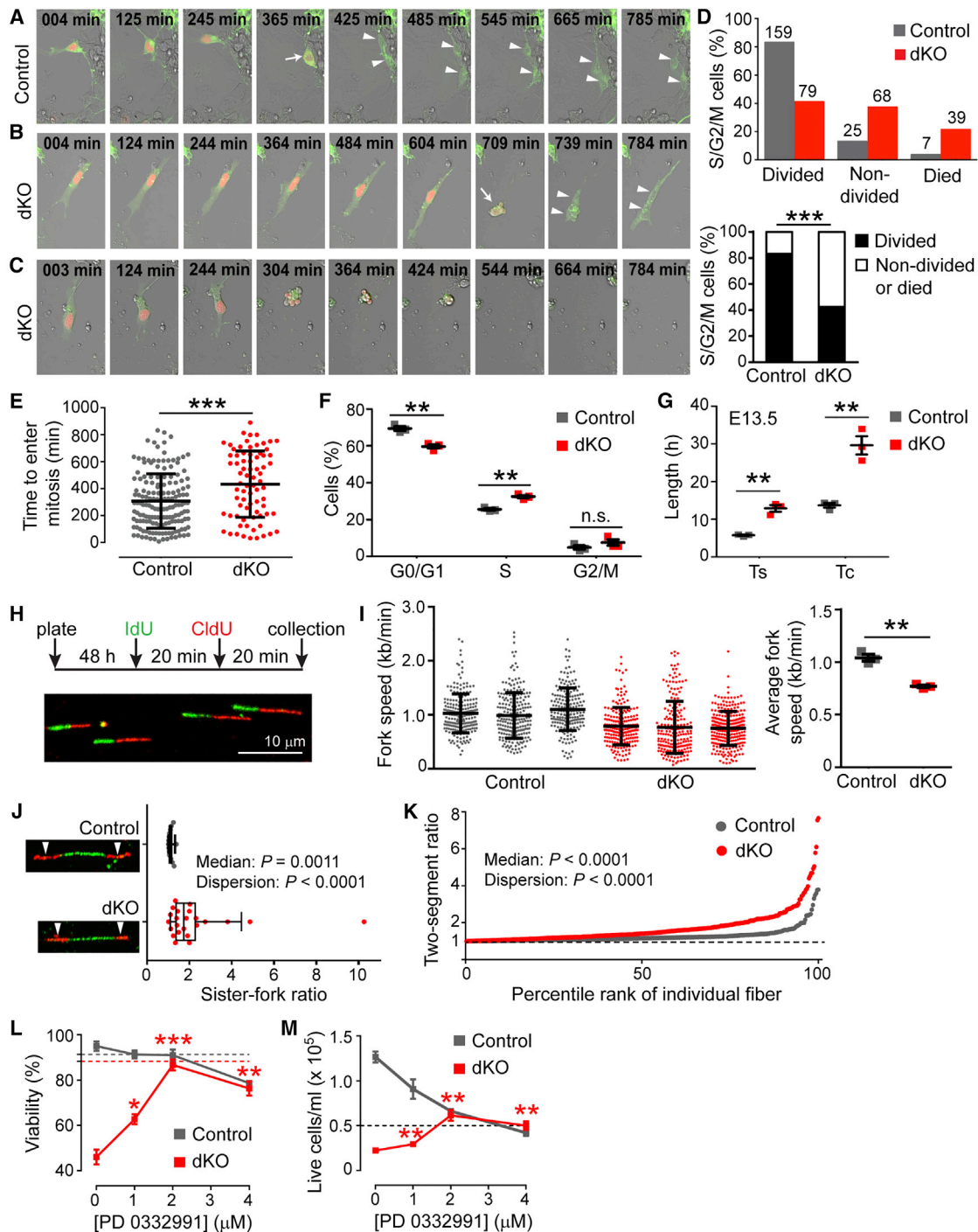


**Figure 5. LATS-Deficient NSCs Exhibit Prolonged S Phase and DNA Replication Stress.**

(A–C) Live imaging snapshots of Fucci-labeled NSCs showing division (A and B) and death (C). Arrows indicate cell rounding at the start of mitosis; arrowheads show the daughter cells.

(D) Quantification of cell behaviors observed by live imaging. The number above each bar in the upper panel is the cell number. Fisher's exact test was used in the lower panel.

(E) Quantification of the time interval between the beginning of imaging and the start of mitosis (mean  $\pm$  SD).

(F) PI analysis of cell-cycle profiles (mean  $\pm$  SEM).

(G) Quantification of Ts and Tc of E13.5 RGCs *in vivo* by cumulative EdU/BrdU labeling (mean  $\pm$  SEM).

(H) Top: diagram of DNA fiber assay. Bottom: representative images of DNA fibers.

(I) Left panel: replication fork speeds of individual fibers (mean  $\pm$  SD). Right panel: average fork speeds for each culture (mean  $\pm$  SEM).

(legend continued on next page)

### LATS-Deficient NSCs Exhibit Prolonged S Phase and DNA Replication Stress

To uncover the cellular defects of *Lats1/2* dKO NSCs, we first observed their behavior directly by live imaging. We transfected NSCs with a modified Fucci plasmid that labels the plasma membrane of all transfected cells green and the nuclei of those in the S/G2/M phases orange (Sakaue-Sawano et al., 2008) and focused on cells displaying orange fluorescence at the beginning of the 14-hr imaging period (Figures 5A–5C; Videos S1, S2, S3, and S4). Of the 191 control NSCs analyzed, most divided within the imaging period, and only a small fraction did not divide or died (Figures 5D and S5A). In contrast, of the 186 dKO NSCs analyzed, fewer than half divided. Moreover, among the cells that divided, it took significantly longer for dKO cells than for control cells to enter mitosis (indicated by cell rounding; arrows in Figures 5A and 5B) (Figure 5E), suggesting that the S/G2 phases were extended in dKO cells. We further assessed the cell-cycle phases by measuring the DNA content by propidium iodide (PI) staining and flow cytometry. A larger fraction of dKO cells than of control cells was in S phase, whereas the fraction of cells in G2/M phases was similar for control and dKO cells (Figure 5F), consistent with an extended S phase. We then quantified the *in vivo* cell-cycle length of E13.5 RGCs by the cumulative EdU/BrdU-labeling method described above (Figure 1D). In contrast to the effects at E12.5, both Ts and Tc were extended in dKO RGCs at E13.5 (Figure 5G), corroborating the results obtained with cell cultures.

To assess the relevance of the S-phase extension, we examined its response to *p53* and *Yap;Taz* deletion. Cre-transfected *Lats1/2<sup>F/F</sup>* cells, when compared to control mCherry transfection, showed cell-cycle profile changes similar to those seen in *Lats1/2* dKO cells: an increase in the S-phase fraction, no change in the G2/M fraction, and a corresponding decrease in the G0/G1 fraction (Figure S5C). Deleting *p53* did not affect these changes, whereas deleting *Yap;Taz* erased them (Figure S5C). These results indicate that the S-phase extension is not secondary to *p53* activation; thus, it may be a relevant cellular phenotype linking YAP/TAZ activation to *p53* activation.

The prolonged S phase of LATS-deficient NSCs prompted the hypothesis that they had defects in DNA replication. This was reinforced by the notion that genes driving cell proliferation often induce DNA replication stress (Macheret and Halazonetis, 2015). To test this, we measured replication fork speeds with a DNA fiber assay that involves labeling progressing replication forks via sequential incorporation of two nucleotide analogs (Figure 5H) (Nieminuszczy et al., 2016). The average fork speed of dKO NSCs was less than that of control cells (Figure 5I), which is indicative of replication stress. Another indication of replication stress is increased asymmetry between sister forks emanating in

opposite directions from the same origin (Figure 5J, arrowheads). Normally, these sister forks tend to travel at similar speeds. Thus, their length ratio (the length of the longer fork divided by that of the shorter one) is close to 1, as was the case in control cells (Figure 5J). Under replication stress, fork stalling and collapse affect the sister forks independently, causing asymmetry in the sister-fork length (ratio > 1). Indeed, sister-fork asymmetry was greatly increased in dKO cells, with both the median and dispersion of sister-fork ratios being significantly larger (Figure 5J). We obtained similar results by calculating the length ratios of the two labeled segments in one fiber (image in Figure 5H): whereas the vast majority of fibers in control cells had a ratio close to 1, the median and dispersion of the ratios in dKO cells were significantly increased (Figure 5K). These results indicate that *Lats1/2* dKO NSCs experience replication stress. Moreover, preventing replication stress by blocking S-phase entry with a CDK4/6 inhibitor (Toogood et al., 2005) significantly increased the viability and cell number of dKO NSCs (Figures 5L and 5M), whereas replication-stress inducers reduced the viability and cell number and induced DNA damage in WT NSCs (Figures S5D and S5E), suggesting that replication stress contributes to the defects of *Lats1/2* dKO NSCs.

### Hypertranscription Contributes to Defects of LATS-Deficient NSCs

We next investigated the potential mechanistic link between YAP/TAZ activation and replication stress. Given that YAP/TAZ are potent transcription activators, we were intrigued by reports that increased global transcription activity, also known as hypertranscription (Percharde et al., 2017a), could induce replication stress (Kotsantis et al., 2016; Stork et al., 2016). Therefore, we monitored the global transcription activity in control and *Lats1/2* dKO NSCs. We quantified nascent RNA synthesis by using nuclear incorporation of 5-ethynyluridine (EU) for 1 hr (Jao and Salic, 2008) and found that RNA synthesis was significantly elevated in dKO cells (Figures 6A and 6B). This increase was not affected by the additional removal of *p53* but was eliminated by the additional removal of *Yap;Taz* (Figure 6C), indicating that hypertranscription was induced by YAP/TAZ activation and was upstream or independent of *p53* activation. Fast-proliferating cells often have elevated RNA synthesis (Percharde et al., 2017a); however, this cannot be why RNA synthesis was higher in *Lats1/2* dKO cells because they proliferated more slowly than control cells.

To determine whether hypertranscription was causally involved in the defects of *Lats1/2* dKO NSCs, we inhibited transcription with an elongation inhibitor, DRB (Bensaude, 2011). After 24 hr of DRB treatment, the viability and cell number of control NSCs were reduced as expected, but, remarkably, those of dKO

(J) Boxplot of sister-fork ratios (the longer sister fork divided by the shorter one). Bars: median values; boxes: 25<sup>th</sup>–75<sup>th</sup> percentiles; whiskers: 10<sup>th</sup>–90<sup>th</sup> percentiles. Arrowheads: sister forks.

(K) Two-segment ratios (the longer segment of each DNA fiber divided by the shorter one) arranged in increasing order.

(L) Viability dose-response curve for sorted live NSCs treated with the CDK4/6 inhibitor PD 0332991 for 24 hr (mean ± SEM). Dashed lines indicate NSC viabilities at 0 hr.

(M) Cell number dose-response curve for sorted live NSCs treated with the CDK4/6 inhibitor PD 0332991 for 24 hr (mean ± SEM). The dashed line shows the number of live cells plated at 0 hr.

In (J) and (K), the permutation-based Wilcoxon rank-sum test and Ansari-Bradley test were used to compare the median and dispersion, respectively. Comparisons in (L) and (M) are against the results of vehicle-treated dKO NSCs. \**p* < 0.05; \*\**p* < 0.01; \*\*\**p* < 0.001; n.s., not significant. See also Figure S5 and Videos S1, S2, S3, and S4.

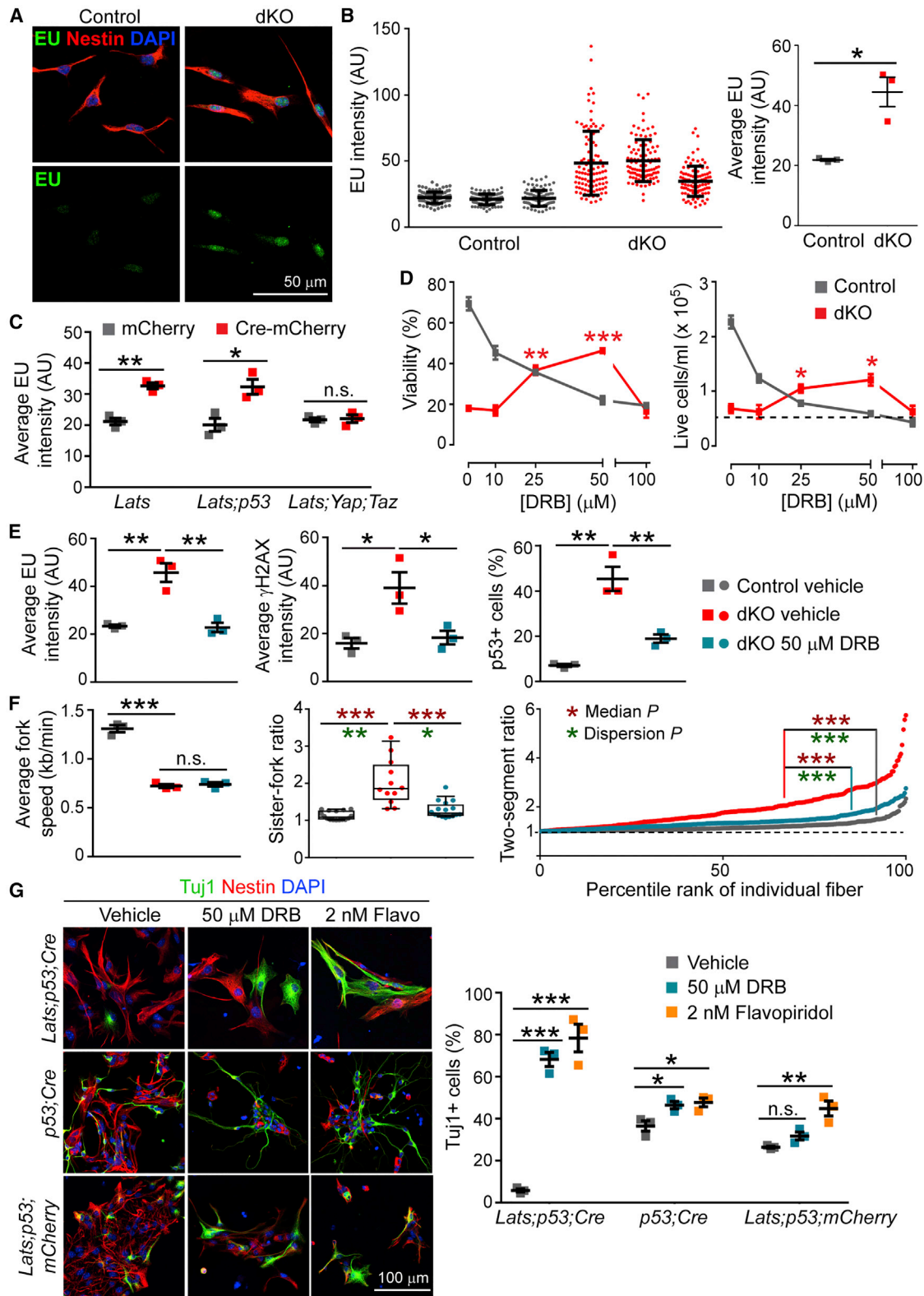


**Figure 6. Hypertranscription Contributes to Defects of LATS-Deficient NSCs**

(A) Representative images of EU staining after 1 hr of labeling.  
(B) Quantification of nuclear EU intensity. Left panel: EU intensity of individual cells (mean  $\pm$  SD). Right panel: average intensity of each culture.  
(C) Average EU intensity of NSCs with the indicated floxed alleles transfected with mCherry or Cre-mCherry plasmid.

(legend continued on next page)

cells increased significantly (Figure 6D). DRB also reduced DNA damage, as detected by  $\gamma$ H2AX staining, and p53 activation in dKO cells (Figure 6E). Replication stress in dKO cells was partially alleviated; although the fork speed was not improved, fork asymmetry was significantly reduced by DRB (Figure 6F). Flavopiridol, another elongation inhibitor, and triptolide, an initiation inhibitor (Bensaude, 2011), also improved the viability and cell number and alleviated replication stress in dKO cells (Figures S6A–S6C). We then tested whether hypertranscription was also involved in the differentiation defect of dKO cells. For this experiment, we used Cre-transfected *Lats1/2<sup>F/F</sup>;p53<sup>F/F</sup>* NSCs to avoid the complication of cell death. These cells failed to differentiate when grown in differentiation medium (Figure 6G), similar to *Lats1/2* dKO NSCs (Figure 4B). Both DRB and flavopiridol greatly enhanced neuronal differentiation of these cells, although they had only mild effects on control (*p53<sup>F/F</sup>;Cre* and mCherry-transfected *Lats1/2<sup>F/F</sup>;p53<sup>F/F</sup>*) cells (Figure 6G), indicating that they are not strong differentiation inducers per se. Together, these data suggest that YAP/TAZ-induced hypertranscription is an important cause of LATS-deficiency phenotypes.

Despite the increase in nascent transcription, protein synthesis was not elevated in *Lats1/2* dKO NSCs (Figure S6D), possibly because of the slower proliferation rate of dKO cells. Interestingly, EU pulse labeling in WT E14.5 embryos revealed markedly higher levels of RNA synthesis in RGCs than in differentiating neurons (Figure S6E), raising the possibility that YAP/TAZ contribute to the high levels of RGC transcription during normal development.

### Global Transcriptome Shift in LATS-Deficient Brains

To further verify the presence of hypertranscription in LATS-deficient NPCs *in vivo* and to determine the scope of the transcriptional changes, we performed CNN RNA-seq (Percharde et al., 2017b) of E12.5 brains. At this stage, the morphologic differences between control and *Lats1/2;Nestin-Cre* dKO brains were subtle, and cell death, DNA damage, and p53 activation were undetectable in dKO brains by immunostaining (Figure S2A). We collected equal numbers of cells from control and dKO telencephalons and added equal amounts of synthetic External RNA Controls Consortium (ERCC) spike-in poly(A) RNAs before RNA extraction. The total RNA yield of dKO cells was significantly higher than that of control cells (Figure 7A). Consistent with this, RNA-seq read counts showed that the fraction of ERCC reads among the total reads was larger in control than in dKO samples (Figure S7A). However, control and dKO brains expressed similar numbers of genes, regardless of whether the expressed genes were defined as those having at least 1 count per million (cpm) RNA-seq reads (Figure 7B) or as those having the promoter chromatin mark H3K4me3 within 5 kb of the transcription start site (TSS) (Figure S7B).

To compare the effects of ERCC normalization and conventional read-depth normalization, we generated heatmaps of

data obtained with both methods (Figure 7C). Whereas read-depth normalization detected similar numbers of up- and downregulated genes in dKO versus control brains, ERCC normalization revealed that many genes were upregulated in dKO brains and only a few were downregulated. An MA plot of significantly changed genes (false discovery rate [FDR] < 0.05) called by ERCC normalization also shows a clear global increase in transcript levels (Figure 7D and Table S2).

Next, we employed NanoString technology to directly quantify gene expression differences in another set of equal numbers of control and dKO telencephalic cells without an enzymatic reaction, such as amplification (Geiss et al., 2008). The raw NanoString counts showed that most of the 770 genes in the NanoString panel were upregulated, whereas normalizing the raw counts to housekeeping genes resulted in similar numbers of up- and downregulated genes (Figure 7E). The trends of changes detected by CNN RNA-seq and NanoString correlated well (Figure 7F). These results validated the global upregulation of transcript levels in *Lats1/2* dKO brains.

To exclude the possibility that the increased RNA levels were simply due to increased RNA stability in dKO cells, we analyzed intron reads because regulation of RNA stability affects mature mRNAs but should not affect intron levels (Wu and Brewer, 2012). Intron levels were globally elevated in dKO cells (Figures S7D and S7E). RNA splicing in dKO cells was normal (Figure S7F), indicating that the intron level increase was not due to abnormal intron retention. These results further confirmed the presence of hypertranscription in *Lats1/2* dKO brains.

### Many Genes Associated with Increased Biosynthetic Capacity and Proliferation Are Upregulated in LATS-Deficient Brains

To determine what types of genes were upregulated in dKO brains, we performed Gene Ontology (GO) analysis of those genes with FDR < 0.01 by using Enrichr (Chen et al., 2013; Kuleshov et al., 2016). The 4,268 upregulated genes ( $\log_2$ -fold change [ $\log_2$ FC] > 0.5) based on ERCC normalization (ERCC-4268) showed significant enrichment of terms for rRNA processing, translation, DNA replication, cell cycle, etc. (Figure 7G and Table S2). In contrast, none of these terms were enriched in the 522 upregulated genes ( $\log_2$ FC > 0.5) based on read-depth normalization (RD-522), and the most significantly enriched terms were ECM organization, Hippo signaling, and EMT, which is consistent with published reports (Lee et al., 2016; Su et al., 2015) (Figure 7G and Table S2). GO analysis of the 550 most strongly upregulated genes ( $\log_2$ FC > 1) by ERCC normalization, ERCC-550, found terms similar to those found by RD-522 (Table S2), which is not surprising because these two sets largely overlap (Figure S7C). These analyses indicate that YAP/TAZ activation upregulates a large set of genes associated with cell growth and proliferation. This effect is not detected by

(D) Dose-response curves for NSCs treated with the transcription inhibitor DRB for 24 hr. Comparisons are against the results of vehicle-treated dKO NSCs. The dashed line shows the number of live cells plated at 0 hr.

(E) Effects of treating dKO NSCs with DRB on EU incorporation,  $\gamma$ H2AX, and p53 activation.

(F) Effects of treating dKO NSCs with DRB on the replication fork speeds, sister-fork ratios, and two-segment ratios. For the fork ratios, Wilcoxon rank-sum test and Ansari-Bradley test were used to compare the median and dispersion, respectively.

(G) Immunostaining and quantification of NSCs of the indicated genotypes grown in differentiation medium with transcription inhibitors for 3 days.

Data are shown as mean  $\pm$  SEM unless otherwise noted; \*p < 0.05; \*\*p < 0.01; \*\*\*p < 0.001; n.s., not significant. See also Figure S6.

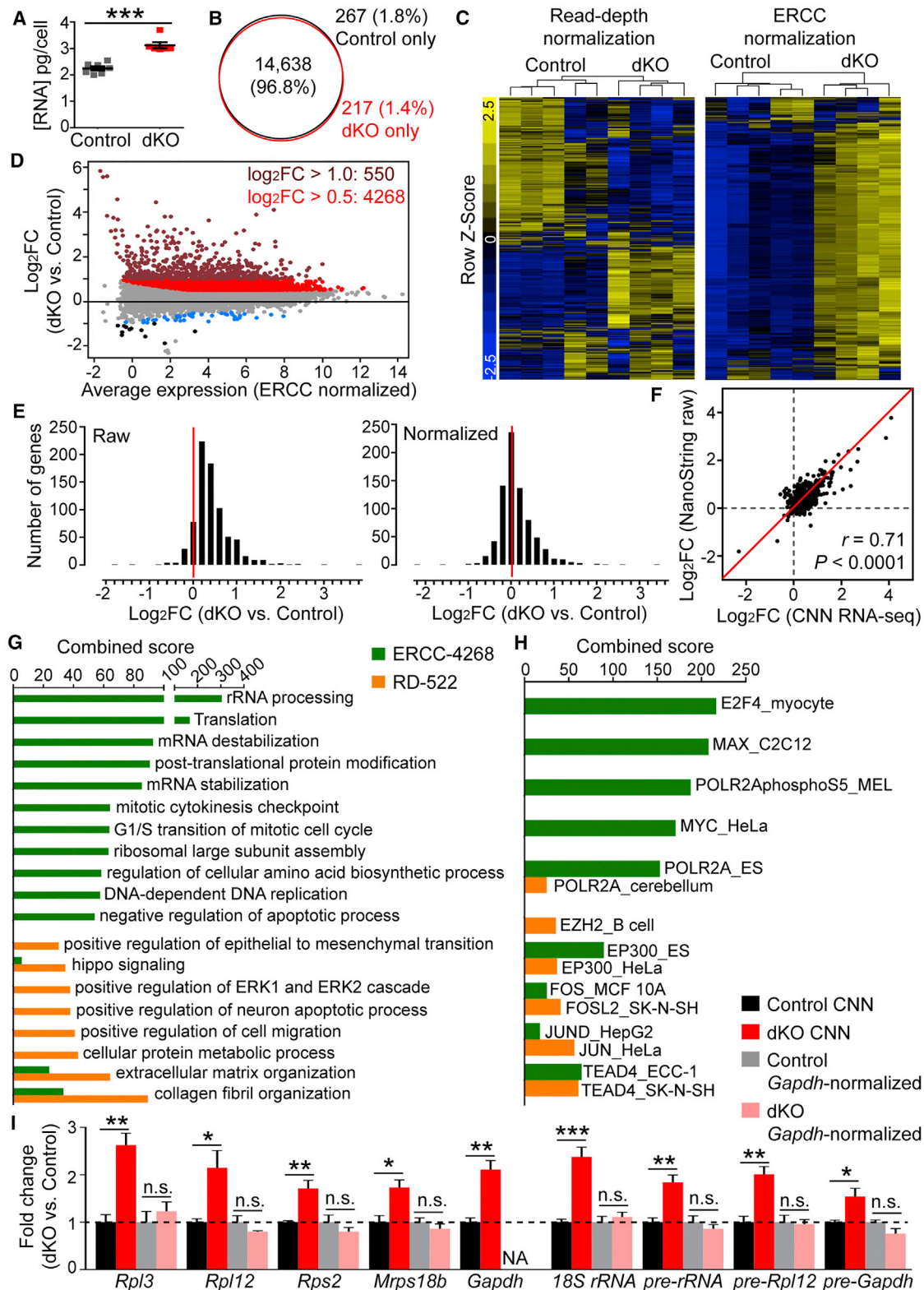


**Figure 7. CNN RNA-Seq Reveals Global Transcriptome Shift in LATS-Deficient Brains.**

(A) Quantification of total RNA content per cell for E12.5 control and *Lats1/2;Nestin-Cre* dKO telencephalic cells (mean ± SEM).

(B) Venn diagram showing overlap of expressed genes defined by having at least 1 cpm RNA-seq reads in E12.5 control and dKO brains.

(C) Gene expression heatmaps for the top 3,000 genes that were most varied in read-depth-normalized and ERCC-normalized data.

(legend continued on next page)

traditional read-depth normalization or by focusing on the most strongly upregulated genes, underscoring the importance of using appropriate normalization methods and analyzing the whole set of changed genes when global transcriptome shifts are present.

ERCC normalization revealed that more than 100 cytoplasmic and mitochondrial ribosomal protein genes were upregulated in dKO brains (Table S2). We performed CNN qRT-PCR for some of these genes and confirmed their upregulation (Figure 7I). These changes were undetectable when *Gapdh* was used for qRT-PCR normalization. In fact, both CNN RNA-seq and CNN qRT-PCR detected upregulation of *Gapdh* in dKO (Table S2 and Figure 7I). CNN qRT-PCR also detected upregulation of 18S rRNA and several primary (unspliced) Pol I and Pol II transcripts in dKO. Changes in rRNA levels could not be detected by our RNA-seq approach because rRNAs were depleted during library preparation.

YAP/TAZ and TEAD predominantly bind distal enhancers rather than promoters (Galli et al., 2015; Stein et al., 2015). They cooperate with other TFs such as AP-1 (a dimer of JUN and FOS) and Myc (Crocì et al., 2017; Stein et al., 2015; Zancato et al., 2015). To gain insights into the transcriptional mechanism underlying hypertranscription in dKO brains, we examined the results of a TF-Target-gene enrichment analysis performed by Enrichr based on ENCODE TF chromatin immunoprecipitation sequencing (ChIP-seq) data (Chen et al., 2013). Surprisingly, the ERCC-4268 gene set showed extraordinary overlap with E2F and Myc-Max targets (Figure 7H and Table S2). Ingenuity pathway analysis of ERCC-4268 also identified Myc as the top upstream regulator ( $p = 2.93E-81$ ). These results agree with a report that Myc and YAP-TEAD coordinately regulate genes required for cell proliferation (Crocì et al., 2017). Indeed, ERCC-4268 overlaps significantly with the 2,196 genes identified by Crocì et al. (2017) as being upregulated by Myc and YAP co-overexpression in 3T9 fibroblasts (3T9-2196) (843 genes overlap,  $p = 1.5E-29$  by Fisher's exact test). Given that Myc promotes transcriptional amplification or hypertranscription in cancer cells, lymphocytes, and mouse primordial germ cells (Lin et al., 2012; Nie et al., 2012; Percharde et al., 2017b), we investigated whether it was involved in the hypertranscription of *Lats1/2* dKO NSCs. We treated NSCs with a potent Myc inhibitor, 10058-F4 (Yin et al., 2003). Over a wide dosage range, the Myc inhibitor had no effect on NSC viability, cell number, or EU incorporation (Figure S7G), although it did impair the colony morphology, proliferation, and pluripotency marker expression of mouse embryonic stem cells (mESCs), consistent with the reported functions of Myc in mESCs (Smith et al., 2010) (Figures S7H and S7I). These data suggest that Myc is not required for YAP/TAZ-induced hypertranscription. Corroborating this finding, Myc

and Max genes were upregulated less than 2-fold in dKO brains (Table S2 and Figure S7J), whereas in the studies cited above, Myc protein or mRNA levels were elevated more than 10-fold over baseline. Together, these results suggest that many genes upregulated in *Lats1/2* dKO brains are Myc targets; however, their upregulation does not depend on Myc when YAP/TAZ are highly activated.

Applying the same TF-Target-gene analysis to the RD-522 and ERCC-550 gene sets revealed significant overlap with TEAD4 and JUN targets, but not with E2F or Myc targets (Figure 7H and Table S2), and there is no significant overlap between them and 3T9-2196 ( $p > 0.1$ ). ERCC-4268 also significantly overlaps with TEAD4 and JUN targets, but to a much lesser degree than with E2F and Myc targets (Figure 7H and Table S2). Because Enrichr predicts and ranks target genes based on the distance of the TF ChIP-seq peaks from the TSS (Chen et al., 2013), it preferentially identifies TF-Target-gene pairs in which the TF binds close to the TSS of the target gene. Therefore, these results suggest that the genes that were strongly upregulated in *Lats1/2* dKO brains (ERCC-550 and RD-522) tend to have TEAD and JUN binding sites near their TSSs. Verteporfin, which disrupts YAP-TEAD interaction (Liu-Chittenden et al., 2012), increased the viability and cell number and lowered nascent transcription of dKO NSCs (Figure S7K), suggesting that TEAD is involved in the hypertranscription of LATS-deficient cells, although this experiment does not indicate whether the upregulated genes were direct TEAD targets.

## DISCUSSION

By studying the effects of *Lats1/2* deletion on mouse brain development, we made two important discoveries. First, YAP/TAZ activation resulting from *Lats1/2* deletion leads to massive apoptosis of NPCs instead of the overgrowth typically associated with YAP/TAZ activation. Second, YAP/TAZ activation leads to hypertranscription and upregulates many genes associated with increased biosynthetic capacity and proliferation. These findings raise several important questions.

First, is hypertranscription a common effect of YAP/TAZ activation? Although microarray and RNA-seq have been routinely used to study transcriptional changes caused by YAP/TAZ activation, these approaches cannot detect global shifts unless appropriate normalization methods are applied (Lovén et al., 2012; Percharde et al., 2017a). By comparing normalization using ERCC spike-in RNAs added based on the cell number with traditional read-depth normalization, we demonstrated that many transcripts are elevated in LATS-deficient brains and that this change cannot be detected by read-depth normalization. Moreover, ERCC normalization revealed upregulation of many

(D) MA plot of differentially expressed genes (FDR < 0.05). Colored dots highlight genes with FDR < 0.01 and with the following fold changes (FCs): maroon,  $\log_2FC > 1$ ; red,  $\log_2FC > 0.5$ ; blue,  $\log_2FC < -0.5$ ; black,  $\log_2FC < -1$ .

(E) Histograms showing gene expression changes in E12.5 dKO telencephalic cells relative to equal numbers of control cells as measured by NanoString without normalization (left panel) or after normalization to housekeeping genes (right panel).

(F) Comparison of NanoString and CNN RNA-seq data. Pearson correlation analysis.

(G) Top GO Biological Processes terms enriched in the ERCC-4268 and RD-522 gene sets.

(H) Top transcription factors whose targets (predicted based on ENCODE ChIP-seq data) were enriched in the ERCC-4268 and RD-522 gene sets.

(I) qRT-PCR analysis of some of the upregulated genes identified by CNN RNA-seq (mean  $\pm$  SEM).

\* $p < 0.05$ ; \*\* $p < 0.01$ ; \*\*\* $p < 0.001$ ; n.s., not significant. See also Figure S7 and Tables S2 and S3.

genes associated with cell growth and the cell cycle, consistent with the known function of YAP/TAZ in promoting proliferation, whereas read-depth normalization detected mainly changes in genes involved in ECM organization and EMT. Thus, our approach yielded insights into YAP/TAZ function. We propose that similar approaches be used to reassess the transcriptional effects of YAP/TAZ activation in other contexts. For example, is YAP/TAZ-driven hypertranscription present in human tumors showing YAP/TAZ activation? Experiments to address this question must be designed carefully to ensure that any observed global transcriptome shift is not due to differences in the cell state, such as the proliferation rate (Kress et al., 2015).

How does YAP/TAZ activation lead to hypertranscription? YAP/TAZ may directly bind and upregulate many genes. Alternatively, they may bind and upregulate just a few genes that in turn activate many others. Distinguishing between these possibilities is not easy because YAP/TAZ and TEAD mostly bind distal enhancers and accurately assigning distal enhancers to their target genes on a genomic scale is challenging. Nevertheless, our bioinformatic analyses provided some important insights. The genes upregulated in LATS-deficient brains were highly enriched for Myc targets, which is interesting because Myc has been shown to promote transcriptional amplification or hypertranscription (Lin et al., 2012; Nie et al., 2012; Percharde et al., 2017b). YAP/TAZ and Myc both promote transcription elongation by recruiting P-TEFb to its target genes (Galli et al., 2015; Rahl et al., 2010). However, Myc at physiologic levels binds mainly active promoters and starts binding active distal enhancers when overexpressed (Kress et al., 2015), whereas YAP/TAZ and TEAD predominantly bind distal enhancers (Galli et al., 2015; Stein et al., 2015). We propose a model in which many genes involved in cell growth and proliferation are co-regulated by Myc and YAP/TAZ-TEAD, with Myc binding at their promoters and YAP/TAZ-TEAD binding at their distal enhancers. Myc and YAP/TAZ may act synergistically (Crocì et al., 2017) or independently, e.g., by responding to different signals or having different dynamics (early versus late or transient versus long-lasting responses). The mode of interplay between Myc and YAP/TAZ may depend on their respective levels and the cell type. For example, although our data suggest that Myc is not required for YAP/TAZ-induced hypertranscription in LATS-deficient NSCs, it might be required when YAP/TAZ levels are lower or in other cell types.

What are the cellular consequences of YAP/TAZ-induced hypertranscription? Based on our finding that the upregulated genes are highly enriched for those associated with increased cell growth and the cell cycle, we propose that hypertranscription is a mechanism by which YAP/TAZ activation drives proliferation. Indeed, LATS-deficient NPCs exhibit an accelerated cell cycle, albeit transiently. The upregulated genes are also enriched for those associated with negative regulation of the apoptotic process (Figure 7G and Table S2), consistent with the established role of YAP/TAZ in promoting cell survival. In NPCs, however, hypertranscription eventually leads to DNA replication stress, DNA damage, and apoptosis. These detrimental effects might result from the induction of specific genes. Alternatively, elevated transcription activity itself could exacerbate the conflicts between replication and transcription as the two large machineries move along the same DNA template in proliferating

cells, causing replication stress and DNA damage (Hamperl and Cimprich, 2016). The response of a given cell type to YAP/TAZ-induced hypertranscription most likely depends on how well that cell type handles and tolerates transcription-replication conflicts, replication stress, and DNA damage. NPCs are particularly sensitive to DNA damage, and their threshold for activating apoptosis is very low (McKinnon, 2017), which is probably why NPCs undergo cell death despite the upregulation of anti-apoptotic genes. Hypertranscription may trigger replication stress and DNA damage in other cell types, e.g., the *Lats1/2*-deficient adult hepatocytes that show increased senescence and death (Lee et al., 2016). On the other hand, in tumors with YAP/TAZ activation, hypertranscription may promote tumor progression by driving proliferation and survival and by inducing replication stress, the latter of which in turn generates genomic instability and selects for escape from apoptosis (Macheret and Halazonetis, 2015).

Lastly, how are LATS and YAP/TAZ regulated under physiologic and pathologic conditions? Our data suggest that in early stages of brain development, LATS are kept on and YAP/TAZ are largely shut off. However, this dynamic may change at different developmental stages or in different regions of the nervous system. Indeed, P0 *Lats1/2;Yap;Taz* KO cortices are thinner than control cortices and contain fewer RGCs (Figures 3A–3C and S3A), which may reflect a requirement for YAP/TAZ in later stages of brain development. The Hippo pathway core components are regulated by a wide range of signals and cellular processes (Meng et al., 2016). Although this suggests that the Hippo pathway can sense and integrate diverse types of signals, the relative impact of these signals on YAP/TAZ activity almost certainly depends on the cell type and physiologic conditions. Much work is needed if we are to obtain a clear and comprehensive understanding of the operational logic behind this complex signaling network centered around YAP/TAZ regulation.

## STAR★METHODS

Detailed methods are provided in the online version of this paper and include the following:

- KEY RESOURCES TABLE
- CONTACT FOR REAGENT AND RESOURCE SHARING
- EXPERIMENTAL MODEL AND SUBJECT DETAILS
  - Mice
  - Neural Stem Cell (NSC) Cultures
  - Mouse Embryonic Stem Cell (ESC) Cultures
- METHOD DETAILS
  - Plasmids
  - Quantitative Western Blot and Subcellular Fractionation
  - *In Utero* Electroporation
  - Histology, Immunostaining, TUNEL Assay, and Image Acquisition
  - Image Quantifications
  - Calculation of *In Vivo* Cell Cycle Parameters
  - NSC Culture Assays
  - Live Imaging of NSCs
  - DNA Fiber Assay and Data Analysis
  - Affymetrix Microarray and Data Analysis

- Cell Number Normalized (CNN) RNA-Seq and Data Analysis
- NanoString Analysis
- CNN qRT-PCR
- Chromatin Immunoprecipitation and Sequencing (ChIP-Seq) and Data Analysis
- QUANTIFICATION AND STATISTICAL ANALYSIS
- DATA AND SOFTWARE AVAILABILITY

## SUPPLEMENTAL INFORMATION

Supplemental Information includes seven figures, three tables, and four videos and can be found with this article online at <https://doi.org/10.1016/j.devcel.2018.09.021>.

## ACKNOWLEDGMENTS

We thank Dr. Richard Ashmun, Dr. Jennifer Peters, Jim Houston, Maria Kinsey, the Flow Cytometry & Cell Sorting facility, the Hartwell Center, and the Cell & Tissue Imaging Center at St. Jude Children's Research Hospital for assistance with data acquisition and analysis. We thank Dr. Young-Goo Han for suggestions regarding the manuscript, Dr. Keith A. Laycock for scientific editing of the manuscript, and Joshua Stokes and Jessica Anderson for assistance with graphic design. A.L., J.Y.P., J.P., R.P.K., and X.C. are supported by R01 NS086938 and American Lebanese Syrian Associated Charities.

## AUTHOR CONTRIBUTIONS

A.L. performed most experiments. J.Y.P. performed initial analysis of *Lats1/2* dKO brains and *in utero* electroporation. J.P. performed western blots and qRT-PCR. D.F., B.X., and Y.F. analyzed RNA-seq and ChIP-seq data. R.P.K. performed ChIP-seq. G.N. analyzed microarray data. H.P. conducted statistical tests of DNA fiber ratios. Y.D.K. and P.J.M. advised on DNA damage. R.L.J. provided *Lats1<sup>F</sup>* and *Lats2<sup>F</sup>* mice. Each experimenter analyzed his own data. X.C. conceived and supervised the project and wrote the manuscript with input from co-authors.

## DECLARATION OF INTERESTS

The authors declare no competing interests.

Received: March 8, 2018

Revised: July 24, 2018

Accepted: September 25, 2018

Published: October 25, 2018

## REFERENCES

Anders, S., Pyl, P.T., and Huber, W. (2015). HTSeq—a python framework to work with high-throughput sequencing data. *Bioinformatics* *31*, 166–169.

Bensaude, O. (2011). Inhibiting eukaryotic transcription: which compound to choose? How to evaluate its activity? *Transcription* *2*, 103–108.

Bylund, M., Andersson, E., Novitsch, B.G., and Muhr, J. (2003). Vertebrate neurogenesis is counteracted by Sox1-3 activity. *Nat. Neurosci.* *6*, 1162–1168.

Cai, J., Maitra, A., Anders, R.A., Taketo, M.M., and Pan, D. (2015).  $\beta$ -catenin destruction complex-independent regulation of Hippo-YAP signaling by APC in intestinal tumorigenesis. *Genes Dev.* *29*, 1493–1506.

Cao, X., Pfaff, S.L., and Gage, F.H. (2008). YAP regulates neural progenitor cell number via the TEA domain transcription factor. *Genes Dev.* *22*, 3320–3334.

Chen, E.Y., Tan, C.M., Kou, Y., Duan, Q., Wang, Z., Meirelles, G.V., Clark, N.R., and Ma'ayan, A. (2013). Enrichr: interactive and collaborative HTML5 gene list enrichment analysis tool. *BMC Bioinformatics* *14*, 128.

Chen, Q., Zhang, N., Xie, R., Wang, W., Cai, J., Choi, K.S., David, K.K., Huang, B., Yabuta, N., Nojima, H., et al. (2015). Homeostatic control of Hippo signaling activity revealed by an endogenous activating mutation in YAP. *Genes Dev.* *29*, 1285–1297.

Cotton, J.L., Li, Q., Ma, L., Park, J.S., Wang, J., Ou, J., Zhu, L.J., Ip, Y.T., Johnson, R.L., and Mao, J. (2017). YAP/TAZ and Hedgehog coordinate growth and patterning in gastrointestinal mesenchyme. *Dev. Cell* *43*, 35–47.e4.

Croci, O., De Fazio, S., Biagioni, F., Donato, E., Caganova, M., Curti, L., Doni, M., Sberna, S., Aldeghi, D., Biancotto, C., et al. (2017). Transcriptional integration of mitogenic and mechanical signals by Myc and YAP. *Genes Dev.* *31*, 2017–2022.

Dobin, A., Davis, C.A., Schlesinger, F., Drenkow, J., Zaleski, C., Jha, S., Batut, P., Chaisson, M., and Gingeras, T.R. (2013). STAR: ultrafast universal RNA-seq aligner. *Bioinformatics* *29*, 15–21.

Englund, C., Fink, A., Lau, C., Pham, D., Daza, R.A., Bulfone, A., Kowalczyk, T., and Hevner, R.F. (2005). Pax6, Tbr2, and Tbr1 are expressed sequentially by radial glia, intermediate progenitor cells, and postmitotic neurons in developing neocortex. *J. Neurosci.* *25*, 247–251.

Galli, G.G., Carrara, M., Yuan, W.C., Valdes-Quezada, C., Gurung, B., Pepe-Mooney, B., Zhang, T., Geeven, G., Gray, N.S., de Laat, W., et al. (2015). YAP drives growth by controlling transcriptional pause release from dynamic enhancers. *Mol. Cell* *60*, 328–337.

Geiss, G.K., Bumgarner, R.E., Birditt, B., Dahl, T., Dowidar, N., Dunaway, D.L., Fell, H.P., Ferrel, S., George, R.D., Grogan, T., et al. (2008). Direct multiplexed measurement of gene expression with color-coded probe pairs. *Nat. Biotechnol.* *26*, 317–325.

Gorski, J.A., Talley, T., Qiu, M., Puelles, L., Rubenstein, J.L., and Jones, K.R. (2002). Cortical excitatory neurons and glia, but not GABAergic neurons, are produced in the Emx1-expressing lineage. *J. Neurosci.* *22*, 6309–6314.

Gurtan, A.M., Lu, V., Bhutkar, A., and Sharp, P.A. (2012). In vivo structure-function analysis of human Dicer reveals directional processing of precursor miRNAs. *RNA* *18*, 1116–1122.

Hamperl, S., and Cimprich, K.A. (2016). Conflict resolution in the genome: how transcription and replication make it work. *Cell* *167*, 1455–1467.

Heallen, T., Morikawa, Y., Leach, J., Tao, G., Willerson, J.T., Johnson, R.L., and Martin, J.F. (2013). Hippo signaling impedes adult heart regeneration. *Development* *140*, 4683–4690.

Heallen, T., Zhang, M., Wang, J., Bonilla-Claudio, M., Klysiak, E., Johnson, R.L., and Martin, J.F. (2011). Hippo pathway inhibits Wnt signaling to restrain cardiomyocyte proliferation and heart size. *Science* *332*, 458–461.

Hergovich, A., and Hemmings, B.A. (2012). Hippo signalling in the G2/M cell cycle phase: lessons learned from the yeast men and sin pathways. *Semin. Cell Dev. Biol.* *23*, 794–802.

Jao, C.Y., and Salic, A. (2008). Exploring RNA transcription and turnover in vivo by using click chemistry. *Proc. Natl. Acad. Sci. USA* *105*, 15779–15784.

Kim, J., Kim, Y.H., Kim, J., Park, D.Y., Bae, H., Lee, D.H., Kim, K.H., Hong, S.P., Jang, S.P., Kubota, Y., et al. (2017). YAP/TAZ regulates sprouting angiogenesis and vascular barrier maturation. *J. Clin. Invest.* *127*, 3441–3461.

Kotsantis, P., Silva, L.M., Irmischer, S., Jones, R.M., Folkes, L., Gromak, N., and Petermann, E. (2016). Increased global transcription activity as a mechanism of replication stress in cancer. *Nat. Commun.* *7*, 13087.

Kress, T.R., Sabò, A., and Amati, B. (2015). MYC: connecting selective transcriptional control to global RNA production. *Nat. Rev. Cancer* *15*, 593–607.

Kriegstein, A., and Alvarez-Buylla, A. (2009). The glial nature of embryonic and adult neural stem cells. *Annu. Rev. Neurosci.* *32*, 149–184.

Kuleshov, M.V., Jones, M.R., Rouillard, A.D., Fernandez, N.F., Duan, Q., Wang, Z., Koplev, S., Jenkins, S.L., Jagodnik, K.M., Lachmann, A., et al. (2016). Enrichr: a comprehensive gene set enrichment analysis web server 2016 update. *Nucleic Acids Res.* *44*, W90–W97.

Lavado, A., He, Y., Paré, J., Neale, G., Olson, E.N., Giovannini, M., and Cao, X. (2013). Tumor suppressor Nf2 limits expansion of the neural progenitor pool by inhibiting Yap/Taz transcriptional coactivators. *Development* *140*, 3323–3334.

Law, C.W., Chen, Y., Shi, W., and Smyth, G.K. (2014). Voom: precision weights unlock linear model analysis tools for RNA-seq read counts. *Genome Biol.* *15*, R29.

Lee, D.H., Park, J.O., Kim, T.S., Kim, S.K., Kim, T.H., Kim, M.C., Park, G.S., Kim, J.H., Kuninaka, S., Olson, E.N., et al. (2016). LATS-YAP/TAZ controls

- lineage specification by regulating TGF $\beta$  signaling and Hnf4 $\alpha$  expression during liver development. *Nat. Commun.* 7, 11961.
- Lin, C.Y., Lovén, J., Rahl, P.B., Paranal, R.M., Burge, C.B., Bradner, J.E., Lee, T.I., and Young, R.A. (2012). Transcriptional amplification in tumor cells with elevated c-Myc. *Cell* 151, 56–67.
- Liu-Chittenden, Y., Huang, B., Shim, J.S., Chen, Q., Lee, S.J., Anders, R.A., Liu, J.O., and Pan, D. (2012). Genetic and pharmacological disruption of the TEAD-YAP complex suppresses the oncogenic activity of YAP. *Genes Dev.* 26, 1300–1305.
- Lovén, J., Orlando, D.A., Sigova, A.A., Lin, C.Y., Rahl, P.B., Burge, C.B., Levens, D.L., Lee, T.I., and Young, R.A. (2012). Revisiting global gene expression analysis. *Cell* 151, 476–482.
- Macheret, M., and Halazonetis, T.D. (2015). DNA replication stress as a hallmark of cancer. *Annu. Rev. Pathol.* 10, 425–448.
- McKinnon, P.J. (2017). Genome integrity and disease prevention in the nervous system. *Genes Dev.* 31, 1180–1194.
- Mello, S.S., and Attardi, L.D. (2018). Deciphering p53 signaling in tumor suppression. *Curr. Opin. Cell Biol.* 51, 65–72.
- Meng, Z., Moroishi, T., and Guan, K.L. (2016). Mechanisms of Hippo pathway regulation. *Genes Dev.* 30, 1–17.
- Nguyen, L., Besson, A., Heng, J.I., Schuurmans, C., Teboul, L., Parras, C., Philpott, A., Roberts, J.M., and Guillemot, F. (2006). p27<sup>Kip1</sup> independently promotes neuronal differentiation and migration in the cerebral cortex. *Genes Dev.* 20, 1511–1524.
- Nie, Z., Hu, G., Wei, G., Cui, K., Yamane, A., Resch, W., Wang, R., Green, D.R., Tessarollo, L., Casellas, R., et al. (2012). c-Myc is a universal amplifier of expressed genes in lymphocytes and embryonic stem cells. *Cell* 151, 68–79.
- Nieminuszczy, J., Schwab, R.A., and Niedzwiedz, W. (2016). The DNA fibre technique—tracking helicases at work. *Methods* 108, 92–98.
- Ota, M., and Sasaki, H. (2008). Mammalian Tead proteins regulate cell proliferation and contact inhibition as transcriptional mediators of Hippo signaling. *Development* 135, 4059–4069.
- Percharde, M., Bulut-Karslioglu, A., and Ramalho-Santos, M. (2017a). Hypertranscription in development, stem cells, and regeneration. *Dev. Cell* 40, 9–21.
- Percharde, M., Wong, P., and Ramalho-Santos, M. (2017b). Global hypertranscription in the mouse embryonic germline. *Cell Rep.* 19, 1987–1996.
- Pettitt, S.J., Liang, Q., Rairdan, X.Y., Moran, J.L., Prosser, H.M., Beier, D.R., Lloyd, K.C., Bradley, A., and Skarnes, W.C. (2009). Agouti C57BL/6N embryonic stem cells for mouse genetic resources. *Nat. Methods* 6, 493–495.
- Pfleger, C.M. (2017). The Hippo pathway: a master regulatory network important in development and dysregulated in disease. *Curr. Top. Dev. Biol.* 123, 181–228.
- Pilaz, L.J., McMahon, J.J., Miller, E.E., Lennox, A.L., Suzuki, A., Salmon, E., and Silver, D.L. (2016). Prolonged mitosis of neural progenitors alters cell fate in the developing brain. *Neuron* 89, 83–99.
- Rahl, P.B., Lin, C.Y., Seila, A.C., Flynn, R.A., McCuine, S., Burge, C.B., Sharp, P.A., and Young, R.A. (2010). c-Myc regulates transcriptional pause release. *Cell* 141, 432–445.
- Reginensi, A., Enderle, L., Gregorieff, A., Johnson, R.L., Wrana, J.L., and McNeill, H. (2016). A critical role for NF2 and the Hippo pathway in branching morphogenesis. *Nat. Commun.* 7, 12309.
- Rogakou, E.P., Nieves-Neira, W., Boon, C., Pommier, Y., and Bonner, W.M. (2000). Initiation of DNA fragmentation during apoptosis induces phosphorylation of H2AX histone at serine 139. *J. Biol. Chem.* 275, 9390–9395.
- Rogakou, E.P., Pilch, D.R., Orr, A.H., Ivanova, V.S., and Bonner, W.M. (1998). DNA double-stranded breaks induce histone H2AX phosphorylation on serine 139. *J. Biol. Chem.* 273, 5858–5868.
- Sakaue-Sawano, A., Kurokawa, H., Morimura, T., Hanyu, A., Hama, H., Osawa, H., Kashiwagi, S., Fukami, K., Miyata, T., Miyoshi, H., et al. (2008). Visualizing spatiotemporal dynamics of multicellular cell-cycle progression. *Cell* 132, 487–498.
- Schmidt, E.K., Clavarino, G., Ceppi, M., and Pierre, P. (2009). SUnSET, a nonradioactive method to monitor protein synthesis. *Nat. Methods* 6, 275–277.
- Schwab, R.A., and Niedzwiedz, W. (2011). Visualization of DNA replication in the vertebrate model system DT40 using the DNA fiber technique. *J. Vis. Exp.* 56, e3255.
- Smith, K.N., Singh, A.M., and Dalton, S. (2010). Myc represses primitive endoderm differentiation in pluripotent stem cells. *Cell Stem Cell* 7, 343–354.
- Stein, C., Bardet, A.F., Roma, G., Bergling, S., Clay, I., Ruchti, A., Agarinis, C., Schmelzle, T., Bouwmeester, T., Schübeler, D., et al. (2015). YAP1 exerts its transcriptional control via TEAD-mediated activation of enhancers. *PLoS Genet.* 11, e1005465.
- Stork, C.T., Bocek, M., Crossley, M.P., Sollier, J., Sanz, L.A., Chédin, F., Swigut, T., and Cimprich, K.A. (2016). Co-transcriptional R-loops are the main cause of estrogen-induced DNA damage. *eLife* 5, e17548.
- Su, T., Bondar, T., Zhou, X., Zhang, C., He, H., and Medzhitov, R. (2015). Two-signal requirement for growth-promoting function of Yap in hepatocytes. *eLife* 4, e02948.
- Subramanian, A., Tamayo, P., Mootha, V.K., Mukherjee, S., Ebert, B.L., Gillette, M.A., Paulovich, A., Pomeroy, S.L., Golub, T.R., Lander, E.S., et al. (2005). Gene set enrichment analysis: a knowledge-based approach for interpreting genome-wide expression profiles. *Proc. Natl. Acad. Sci. USA* 102, 15545–15550.
- Toogood, P.L., Harvey, P.J., Repine, J.T., Sheehan, D.J., VanderWel, S.N., Zhou, H., Keller, P.R., McNamara, D.J., Sherry, D., Zhu, T., et al. (2005). Discovery of a potent and selective inhibitor of cyclin-dependent kinase 4/6. *J. Med. Chem.* 48, 2388–2406.
- Tronche, F., Kellendonk, C., Kretz, O., Gass, P., Anlag, K., Orban, P.C., Bock, R., Klein, R., and Schütz, G. (1999). Disruption of the glucocorticoid receptor gene in the nervous system results in reduced anxiety. *Nat. Genet.* 23, 99–103.
- White, D.E., Negorev, D., Peng, H., Ivanov, A.V., Maul, G.G., and Rauscher, F.J., III (2006). KAP1, a novel substrate for PIKK family members, colocalizes with numerous damage response factors at DNA lesions. *Cancer Res.* 66, 11594–11599.
- Wu, X., and Brewer, G. (2012). The regulation of mRNA stability in mammalian cells: 2.0. *Gene* 500, 10–21.
- Xin, M., Kim, Y., Sutherland, L.B., Qi, X., McAnally, J., Schwartz, R.J., Richardson, J.A., Bassel-Duby, R., and Olson, E.N. (2011). Regulation of insulin-like growth factor signaling by Yap governs cardiomyocyte proliferation and embryonic heart size. *Sci. Signal.* 4, ra70.
- Yin, X., Giap, C., Lazo, J.S., and Prochownik, E.V. (2003). Low molecular weight inhibitors of Myc-Max interaction and function. *Oncogene* 22, 6151–6159.
- Yu, F.X., Zhao, B., and Guan, K.L. (2015). Hippo pathway in organ size control, tissue homeostasis, and cancer. *Cell* 163, 811–828.
- Zanconato, F., Cordenonsi, M., and Piccolo, S. (2016). YAP/TAZ at the roots of cancer. *Cancer Cell* 29, 783–803.
- Zanconato, F., Forcato, M., Battilana, G., Azzolin, L., Quaranta, E., Bodega, B., Rosato, A., Bicciato, S., Cordenonsi, M., and Piccolo, S. (2015). Genome-wide association between YAP/TAZ/TEAD and AP-1 at enhancers drives oncogenic growth. *Nat. Cell Biol.* 17, 1218–1227.
- Zhao, B., Wei, X., Li, W., Udan, R.S., Yang, Q., Kim, J., Xie, J., Ikenoue, T., Yu, J., Li, L., et al. (2007). Inactivation of YAP oncoprotein by the Hippo pathway is involved in cell contact inhibition and tissue growth control. *Genes Dev.* 21, 2747–2761.
- Ziv, Y., Bielopski, D., Galanty, Y., Lukas, C., Taya, Y., Schultz, D.C., Lukas, J., Bekker-Jensen, S., Bartek, J., and Shiloh, Y. (2006). Chromatin relaxation in response to DNA double-strand breaks is modulated by a novel ATM- and KAP-1 dependent pathway. *Nat. Cell Biol.* 8, 870–876.

## STAR★METHODS

### KEY RESOURCES TABLE

REAGENT or RESOURCE	SOURCE	IDENTIFIER
<b>Antibodies</b>		
Mouse monoclonal anti- $\beta$ -Actin (clone AC-15)	Thermo Fisher Scientific	Cat# AM4302; RRID: AB_2536382
Mouse monoclonal anti-BrdU/IdU (clone B44)	BD Biosciences	Cat# 347580; RRID: AB_400326
Rat monoclonal anti-BrdU/CldU [clone BU1/75 (ICR1)]	Abcam	Cat# ab6326; RRID: AB_305426
Rabbit polyclonal anti-Cleaved Caspase-3 (Asp175)	Cell Signaling Technology	Cat# 9661; RRID: AB_2341188
Mouse monoclonal anti- $\beta$ -Catenin (clone L54E2) Alexa Fluor 647 Conjugate	Cell Signaling Technology	Cat# 4627; RRID: AB_10691326
Rat monoclonal anti-Ctip2 (clone 25B6)	Abcam	Cat# ab18465; RRID: AB_2064130
Rabbit polyclonal anti-GFP	Thermo Fisher Scientific	Cat# A-6455; RRID: AB_221570
Rabbit polyclonal anti-phospho-Histone H3 (Ser10)	Millipore	Cat# 06-570; RRID: AB_310177
Rabbit polyclonal anti-trimethyl-Histone H3 (Lys4)	Millipore	Cat# 07-473; RRID: AB_1977252
Rabbit polyclonal anti-phospho-KAP-1 (S824)	Bethyl Labs	Cat# A300-767A; RRID: AB_669740
Rabbit monoclonal anti-Ki67	Vector Laboratories	Cat# VP-RM04; RRID: AB_2336545
Goat polyclonal anti-Nestin	R and D Systems	Cat# AF2736; RRID: AB_416673
Rabbit polyclonal anti-Oct4	Cell Signaling Technology	Cat# 2750; RRID: RRID: AB_823583
Mouse monoclonal anti-p27Kip1	BD Biosciences	Cat# 610241; RRID: AB_397636
Mouse monoclonal anti-p53 (clone 1C12)	Cell Signaling Technology	Cat# 2524; RRID: AB_331743
Rabbit polyclonal anti-PARP	Cell Signaling Technology	Cat# 9542; RRID: AB_2160739
Rabbit polyclonal anti-Pax6 (clone Poly19013)	BioLegend	Cat# 901301; RRID: AB_2565003
Mouse monoclonal anti-Puromycin (clone 12D10)	Millipore	Cat# MABE343; RRID: AB_2566826
Mouse monoclonal anti-SatB2 (clone SATBA4B10)	Abcam	Cat# ab51502; RRID: AB_882455
Rabbit monoclonal anti-Sox2 (clone C70B1)	Cell Signaling Technology	Cat# 3728; RRID: AB_2194037
Mouse monoclonal anti-Sox2 (clone O30-678) Alexa Fluor 488 Conjugate	BD Biosciences	Cat# 561593; RRID: AB_10894382
Rabbit polyclonal anti-Tbr1	Abcam	Cat# ab31940; RRID: AB_2200219
Rabbit polyclonal anti-Tbr2/Eomes	Abcam	Cat# ab23345; RRID: AB_778267
Rat monoclonal anti-Tbr2/Eomes (clone Dan11mag)	Thermo Fisher Scientific	Cat# 14-4875-82; RRID: AB_11042577
Mouse monoclonal anti-acetylated Tubulin (clone 6-11B-1)	Sigma-Aldrich	Cat# T6793; RRID: AB_477585
Mouse monoclonal anti-Tubulin $\beta$ 3 (clone TUJ1)	BioLegend	Cat# 801202; RRID: AB_10063408
Rabbit monoclonal anti-YAP/TAZ (clone D24E4)	Cell Signaling Technology	Cat# 8418; RRID: AB_10950494
Rabbit polyclonal anti-Phospho-YAP (Ser127)	Cell Signaling Technology	Cat# 4911S; RRID: AB_2218913
Rabbit monoclonal anti-Histone H2A.X, phospho (Ser139) (clone 20E3)	Cell Signaling Technology	Cat# 9718; RRID: AB_2118009
Mouse monoclonal anti-ZO-1 (clone ZO1-1A12) Alexa Fluor 488 Conjugate	Thermo Fisher Scientific	Cat# 339188; RRID: AB_2532187
<b>Chemicals, Peptides, and Recombinant Proteins</b>		
10058-F4 (Myc inhibitor)	Sigma-Aldrich	Cat# F3680; CAS: 403811-55-2
DRB (5,6-Dichloro-1- $\beta$ -D-ribofuranosylbenzimidazole)	Sigma-Aldrich	Cat# D1916; CAS: 53-85-0
Flavopiridol	Sigma-Aldrich	Cat# F3055
Triptolide	Calbiochem	Cat# 645900; CAS: 38748-32-2
Verteporfin	Sigma-Aldrich	Cat# SML0534; CAS: 129497-78-5
BrdU (5-Bromo-2'-deoxyuridine)	Sigma-Aldrich	Cat# B5002; CAS: 59-14-3
IdU (Iodoxuridine)	Sigma-Aldrich	Cat# 1336001; CAS: 54-42-2
CldU (5-chloro-2'-deoxyuridine)	Abcam	Cat# ab213715; CAS: 50-90-8
Camptothecin	Calbiochem	Cat# #208925; CAS: 2114454
Etosopside	Tocris	Cat#1226; CAS: 33419-42-0

(Continued on next page)

**Continued**

REAGENT or RESOURCE	SOURCE	IDENTIFIER
Hydroxyurea	Sigma-Aldrich	Cat# H8627; CAS: 127-07-1
PD 0332991 (CDK4/6 inhibitor)	Sigma-Aldrich	Cat# PZ0199; CAS: 827022-33-3
Puromycin	Sigma-Aldrich	Cat# P8833; CAS: 58-58-2
Cyclohexamide	Acros Organics	Cat#357420010; CAS: 66-81-9
Laminin	Corning	Cat# 354232
Poly-L-Lysine	Corning	Cat# 354210
ERCC RNA Spike-In Mix	Thermo Fisher Scientific	Cat# 4456740
Halt Protease and Phosphatase Inhibitor Cocktail (100X)	Thermo Fisher Scientific	Cat# 78440
StemPro Accutase Cell Dissociation Reagent	Thermo Fisher Scientific	Cat# A1110501
N-2 Supplement (100X)	Thermo Fisher Scientific	Cat# 17502048
B-27 Supplement (50X), serum free	Thermo Fisher Scientific	Cat# 17504044
Human FGF-2	Miltenyi Biotec	Cat# 130-093-841
Human EGF	Miltenyi Biotec	Cat# 130-093-825
Horse Serum, heat inactivated	Thermo Fisher Scientific	Cat# 26050088
Embryonic stem-cell FBS	Thermo Fisher Scientific	Cat# 10439024
MEM Non-Essential Amino Acids Solution (100X)	Thermo Fisher Scientific	Cat# 11140050
ESGRO Recombinant Mouse LIF Protein	Millipore Sigma	Cat# ESG1107
Fibronectin	Thermo Fisher Scientific	Cat# PHE0023
Formaldehyde solution	Sigma-Aldrich	Cat# F1635; CAS: 50-00-0
<b>Critical Commercial Assays</b>		
ApopTag Plus In Situ Apoptosis Fluorescein Detection Kit	Millipore	Cat# S7111
Mouse Neural Stem Cell Nucleofector Kit	Lonza	Cat# VPG-1004
NE-PER Nuclear and Cytoplasmic Extraction Reagents	Thermo Fisher Scientific	Cat# 78833
ImmPACT DAB Peroxidase (HRP) Substrate	Vector Laboratories	Cat# SK-4105
Click-it Plus EdU Alexa Fluor 488 Imaging Kit	Thermo Fisher Scientific	Cat# C10637
Click-iT™ RNA Alexa Fluor 488 Imaging Kit	Thermo Fisher Scientific	Cat# C10329
TruSeq Stranded Total RNA Library Prep	Illumina	Cat# 20020597
Quant-iT PicoGreen dsDNA assay	Thermo Fisher Scientific	Cat# P11496
NEBNext ChIP-Seq Library Prep Reagent Set for Illumina	New England Biolabs	Cat# E6200
NEBNext Q5 Hot Start HiFi PCR Master Mix	New England Biolabs	Cat# M0543S
nCounter PanCancer Mouse Pathways Panel	NanoString	Cat # XT-CSO-MPATH1-12
iTaq Universal SYBR Green Supermix	Bio-Rad	Cat# 1725120
SuperScript™ III Reverse Transcriptase	Thermo Fisher Scientific	Cat# 18080093
Dead Cell Removal Kit	Miltenyi Biotec	Cat# 130-090-101
MOM basic kit	Vector Laboratories	Cat# BMK-2202
<b>Deposited Data</b>		
Raw data files for microarray, RNA-seq, and ChIP-seq	This paper	GEO: GSE120016
<b>Experimental Models: Cell Lines</b>		
JM8A3.N1 mouse ES cells	<a href="#">Pettitt et al. (2009)</a>	KOMP: JM8A3.N1
<b>Experimental Models: Organisms/Strains</b>		
Mouse: <i>Nestin-Cre</i> : B6.Cg-Tg(Nes-cre)1Kln/J	The Jackson Laboratory	JAX: 003771
Mouse: <i>Emx1-Cre</i> : B6.129S2- <i>Emx1</i> <sup>tm1(Cre)Krf</sup> /J	The Jackson Laboratory	JAX: 005628
Mouse: <i>p53</i> <sup>flox</sup> ; B6.129P2- <i>Trp53</i> <sup>tm1Bm</sup> /J	The Jackson Laboratory	JAX: 008462
Mouse: <i>Lats1</i> <sup>flox</sup>	<a href="#">Heallen et al. (2011)</a>	N/A
Mouse: <i>Lats2</i> <sup>flox</sup>	<a href="#">Heallen et al. (2011)</a>	N/A
Mouse: <i>Yap</i> <sup>flox</sup>	<a href="#">Xin et al. (2011)</a>	N/A
Mouse: <i>Taz</i> <sup>flox</sup>	<a href="#">Xin et al. (2011)</a>	N/A

(Continued on next page)

**Continued**

REAGENT or RESOURCE	SOURCE	IDENTIFIER
<b>Recombinant DNA</b>		
pCAG3-IRES-EGFP (pCIG3)	This paper	N/A
p2xFlag CMV2-YAP2	<a href="#">Zhao et al. (2007)</a>	Addgene #19045
pCMV-flag YAP2 5SA	<a href="#">Zhao et al. (2007)</a>	Addgene #27371
pCMV-Flag-YAP-5SA/S94A	<a href="#">Zhao et al. (2007)</a>	Addgene #33103
pCIG3-YAP	This paper	N/A
pCIG3-YAP-5SA	This paper	N/A
pCIG3-YAP-5SA/S94A	This paper	N/A
pCAGGS-mCherry	<a href="#">Gurtan et al. (2012)</a>	Addgene #41583
pCAG-Cre-T2A-mCherry	This paper, Solecki DJ	N/A
Fucci plasmid: myr-hmAG1-T2A-hmKQ2-Geminin	This paper, Solecki DJ	N/A
<b>Software and Algorithms</b>		
AxioVision	Zeiss	N/A
NIS-Elements software	Nikon	N/A
ImageJ	NIH	<a href="https://imagej.nih.gov/ij/download.html">https://imagej.nih.gov/ij/download.html</a>
Imaris 9.1	Bitplane	N/A
Zen	Zeiss	N/A
cellSens	Olympus	N/A
ModFit	Verity Software house	N/A
GraphPad Prism 7.04	GraphPad	N/A
Enrichr	<a href="#">Chen et al. (2013)</a> ; <a href="#">Kuleshov et al. (2016)</a>	<a href="http://amp.pharm.mssm.edu/Enrichr/">http://amp.pharm.mssm.edu/Enrichr/</a>
R	R Studio	<a href="https://www.rstudio.com/products/rstudio/download/">https://www.rstudio.com/products/rstudio/download/</a>
STATA/MP 14.2	Stata Corp	N/A
Image Studio Software ver 5.2	LI-COR	N/A
<b>Other</b>		
Corning 60 mm Gridded Scoring Dish	Stem Cell Technologies	Cat# 27500
$\mu$ -Slide 2 Well	ibidi	Cat# 80286
DIC lid for $\mu$ -Slides	ibidi	Cat# 80055

**CONTACT FOR REAGENT AND RESOURCE SHARING**

Further information and requests for resources and reagents may be directed to and will be fulfilled by the Lead Contact, Xinwei Cao ([xinwei.cao@stjude.org](mailto:xinwei.cao@stjude.org)).

**EXPERIMENTAL MODEL AND SUBJECT DETAILS**

**Mice**

The following mouse strains were used: *Lats1<sup>fllox</sup>* and *Lats2<sup>fllox</sup>* ([Heallen et al., 2011](#)), *Nestin-Cre* (JAX stock #003771), *Emx1-Cre* (JAX stock #005628), *p53<sup>fllox</sup>* (JAX stock #008462), and *Yap<sup>fllox</sup>* and *Taz<sup>fllox</sup>* ([Xin et al., 2011](#)). All mice were maintained in a mixed genetic background. All animal procedures were approved by the Institutional Animal Care and Use Committee of St. Jude Children's Research Hospital. Mouse housing and husbandry conditional followed the standards set by the Animal Resource Center at St. Jude Children's Research Hospital. Embryonic (E) day 12–15 and postnatal (P) day 0 mice were used for this study. Their sex was not determined.

**Neural Stem Cell (NSC) Cultures**

Cortices of E12.5 or E13.5 mouse embryos were dissected in cold DMEM/F12. Each culture was derived from an independent embryo. Cells were dissociated with StemPro Accutase (Thermo Fisher Scientific A1110501) and plated at 50,000 cells/ml in petri dishes and grown in NSC maintenance medium composed of DMEM/F12 (Thermo Fisher Scientific 11320033), N2 (Thermo Fisher Scientific 17502048), B27 (Thermo Fisher Scientific 17504044), 20 ng/ml FGF2 (Miltenyi Biotec 130-093-841) and 20 ng/ml EGF (Miltenyi Biotec 130-093-825) at 37°C, 5% CO<sub>2</sub>. After 3 days, neurospheres were dissociated with StemPro Accutase into single cell suspensions and

plated at 50,000 cells/ml in NSC maintenance medium either in petri dishes for neurosphere cultures or on poly-L-Lysine (30  $\mu$ g/ml) and laminin (3  $\mu$ g/ml) coated coverslips for adherent cultures. These cells are considered passage-1 NSCs.

### Mouse Embryonic Stem Cell (ESC) Cultures

JM8A3.N1 mouse ES cells (Pettitt et al., 2009) were grown in DMEM high glucose (Thermo Scientific 11960044) supplemented with 15% FBS (Thermo Scientific 10439024), non-essential amino acids (NEAA) (Thermo Scientific 11140050), L-glutamine (Thermo Scientific 25030081), 0.1 mM 2-mercaptoethanol (Sigma M6145) and 2000 U/ml LIF (Millipore ESG1107) on irradiated mouse embryonic fibroblasts in 12-well plates.

## METHOD DETAILS

### Plasmids

pCAG3-IRES-EGFP (pCIG3) was generated by inserting an MCS-IRES-EGFP cassette into pCAGGS. YAP (Addgene #19045), YAP<sup>5SA</sup> (Addgene #27371), and YAP<sup>5SA/S94A</sup> (Addgene #33103) were gifts from Kun-Liang Guan. The coding sequences were PCR-amplified and inserted into pCIG3. pCAGGS-mCherry (Addgene #41583) was a gift from Phil Sharp. pCAG-Cre-T2A-mCherry and a modified Fucci plasmid (myr-hmAG1-T2A-hmKO2-Geminin) were gifts from David Solecki.

### Quantitative Western Blot and Subcellular Fractionation

E12.5 and E13.5 mouse brains were dissected and total cell lysates were prepared in 20 mM HEPES (pH 7.4), 150 mM NaCl, 2% SDS and 5% glycerol supplemented with AEBSF and Halt protease and phosphatase inhibitors (Thermo Fisher Scientific). Protein concentrations were measured by BCA assay (Thermo Scientific). 20  $\mu$ g of protein per lane were subjected to SDS-PAGE, probed with primary antibodies and infrared conjugated secondary antibodies (LI-COR, IRDye 680LT and 800CW), and detected using the ODYSSEY imaging system (LI-COR). Quantification was performed with Image Studio software ver 5.2 (LI-COR). Cytoplasmic and nuclear fractionation was performed by using the NE-PER Nuclear and Cytoplasmic Extraction Reagents (Thermo Fisher Scientific 78833) according to the manual. For each E13 brain, 200  $\mu$ l of CER I, 11  $\mu$ l of CER II, and 100  $\mu$ l of NER were used. 5% of each fraction was loaded per lane for quantitative Western blots. Each lane in Western blot images and each data point in quantification graphs correspond to an individual embryo.

### In Utero Electroporation

Pregnant mice carrying E12.5 embryos were deeply anesthetized with 2.5–3% of isoflurane and the uterine horns exposed. Approximately 2  $\mu$ l of DNA (2  $\mu$ g/ $\mu$ l) mixed with 0.1% fast green (Sigma) in PBS was injected into a lateral ventricle of the embryo brain using a pulled glass micropipette. Embryo head was placed within a 3-mm tweezer-type electrodes, and square-wave electric pulses (30 V, 50 msec) were delivered 5 times at 950 msec intervals using an electroporator (BTX ECM 830, Harvard Apparatus). Embryos were returned to dam and allowed to resume normal development before being harvested for subsequent analyses.

### Histology, Immunostaining, TUNEL Assay, and Image Acquisition

Mouse brains were dissected in PBS, fixed overnight in 4% paraformaldehyde (PFA) at 4°C, and washed in PBS. For paraffin sections, fixed brains were dehydrated in 70% ethanol overnight, embedded in paraffin, and sectioned at 7- $\mu$ m thickness. For histological analysis, sections were rehydrated and stained with hematoxylin and eosin (H&E). For immunostaining, after rehydration, sections were incubated for 30 min in 10 mM Sodium Citrate (pH 6.0) at 95°C for antigen retrieval. After cooling down at room temperature (RT) for 20 min, sections were washed twice in PBS, blocked and permeabilized in PBS with 3% normal donkey serum and 0.2% Triton X-100 for 1 h, and incubated with primary antibodies at 4 °C overnight. Sections were then washed in PBS 3 times with 15-min intervals and incubated with appropriate fluorescence-conjugated secondary antibodies (Jackson ImmunoResearch Laboratories) at 1:1000 dilution and DAPI (1:1000 dilution) for 2–3 h at RT. After three washes in PBS, sections were coverslipped in ProLong Gold (Thermo Scientific Invitrogen). For DAB (3,3'-diaminobenzidine tetrahydrochloride) staining, a horseradish peroxidase (HRP)-conjugated secondary antibody (Jackson ImmunoResearch Laboratories) was used at 1:250 dilution. After washes in PBS, sections were incubated in the ImmPACT DAB Peroxidase (HRP) Substrate (Vector Laboratories SK-4105) to desired color development and immediately washed in tap water. For frozen sections, fixed brains were cryoprotected in 30% sucrose overnight, embedded in Tissue Freezing Medium (Thermo Scientific), and sectioned at 10–14- $\mu$ m thickness. Immunostaining was carried out as described above without rehydration and antigen retrieval. TUNEL assay was performed using the ApoTag Plus In Situ Apoptosis Fluorescein Detection Kit (Millipore S7111). Images of H&E-stained sections were acquired using a Zeiss Stereo Discovery V8 microscope equipped with an AxiocamMrc camera and processed with Axiovision. Low magnification fluorescent images were acquired using an Olympus BX63 microscope equipped with an Orca Flash4.0 camera. High magnification fluorescent images were acquired using a Zeiss LSM 780 confocal microscope.

### Image Quantifications

All images used for cell counting were acquired using a Zeiss LSM 780 confocal microscope and a 40x objective lens. Cell numbers were counted manually using ImageJ. For each genotype, 3–4 embryos with one section of comparable positions per embryo were quantified. For cortical ventricular zone area measurements at E12.5, images of Pax6 DAB staining were acquired using an Olympus

BX63 microscope. Areas of interest were outlined and measured using the Olympus CellSens Dimension analysis program (Olympus). For each genotype, 3–4 embryos with one section of each rostrocaudal position per embryo were quantified. For quantification of TUNEL, cleaved caspase-3, and Pax6 fluorescent signals, image acquisition was performed below saturation with the same settings for all the samples. The areas containing TUNEL and cleaved caspase-3 signals were measured using the Imaris 9.1 software (Bitplane) and shown as percentages of DAPI+ areas. The areas containing Pax6 signals in the cortex were measured using Imaris and shown as total areas. For each genotype, 3 animals with 8 (E13.5) or 6 (P0) images per animal were analyzed. For quantification of the in utero electroporation experiments, processed image stacks were segmented and GFP+ cells were automatically counted and visually confirmed using Imaris. For each transfection, 3 embryos with one section per embryo were quantified. Data points in all quantification graphs correspond to individual embryos.

### Calculation of *In Vivo* Cell Cycle Parameters

Pregnant dams were injected intraperitoneally with EdU (10  $\mu\text{g/g}$  body weight) and followed by BrdU (50  $\mu\text{g/g}$  body weight) 1.5 h later. Dams were killed at 2 h following EdU administration, and embryos were fixed. EdU was detected by the Click-it Plus EdU Alexa Fluor 488 Imaging Kit (Thermo Scientific Invitrogen), followed by immunostaining with Sox2, Tbr2 and BrdU antibodies. To calculate the cell cycle parameters of RGCs (Sox2+Tbr2 $^-$ ), the total number of Sox2+Tbr2 $^-$  cells (Cycling<sub>fraction</sub>), the number of Sox2+Tbr2 $^-$  cells in the S phase (S<sub>fraction</sub>, Sox2+Tbr2 $^-$ EdU+BrdU $^+$ ) and the number of Sox2+Tbr2 $^-$  cells in the “leaving fraction” (L<sub>fraction</sub>, Sox2+Tbr2 $^-$ EdU+BrdU $^-$ ) were counted manually using ImageJ. S-phase length ( $T_S$ ) and total cell-cycle length ( $T_C$ ) were then calculated using the following equations:

$$\frac{T_S}{T_L} = \frac{S_{\text{fraction}}}{L_{\text{fraction}}} \quad (1)$$

$$T_S = \frac{S_{\text{fraction}}}{L_{\text{fraction}}} \times T_L \quad (2)$$

$$T_S = \frac{S_{\text{fraction}}}{L_{\text{fraction}}} \times 1.5 \quad (3)$$

$$\frac{T_C}{T_S} = \frac{\text{Cycling}_{\text{fraction}}}{S_{\text{fraction}}} \quad (4)$$

$$T_C = \frac{\text{Cycling}_{\text{fraction}}}{S_{\text{fraction}}} \times T_S \quad (5)$$

### *In Vivo* EU Labeling and Detection

A pregnant dam carrying E14.5 embryos was injected intraperitoneally with EU (150  $\mu\text{g/g}$  body weight) and embryos were collected 3 h later (Jao and Salic, 2008). Embryos and the dam were fixed and processed as described above. EU was detected by the Click-it RNA Alexa Fluor 488 Imaging Kit (Thermo Scientific Invitrogen C10329), followed by immunostaining with Pax6, Tbr2 and Ki67 antibodies.

### NSC Culture Assays

All assays were performed on passage-1 NSC cultures.

#### Immunostaining

Free floating neurospheres or NSCs grown on poly-L-Lysine (30  $\mu\text{g/ml}$ ) and laminin (3  $\mu\text{g/ml}$ ) coated coverslips were fixed in 4% PFA for 15 min at RT, permeabilized in PBS with 0.001% Triton X-100 for 10 min, blocked in PBS with 10% fetal calf serum for 30 min, and incubated with primary and secondary antibodies for 1–3 h at RT.

#### Differentiation Assay

Passage-1 NSCs were plated in differentiation medium composed of DMEM/F12, N2, B27, and 5% horse serum (Thermo Fisher Scientific 26050088) at 50,000 cells/ml on poly-L-Lysine and laminin coated coverslips for 1, 3, or 5 days. For differentiation assays in the presence of transcription inhibitors, cells were grown for 3 days and medium was changed every day with fresh inhibitors.

#### Quantification of Neurosphere Numbers and Viability

Neurosphere number was manually counted 3 days after plating using gridded scoring dishes (Stem Cell Technologies 27500). For viability and cell number quantifications, neurospheres were dissociated with StemPro Accutase into single cell suspensions and an aliquot was mixed with trypan blue before being measured by the Countess automated cell counter (Thermo Fisher Scientific).

### **Electroporation**

NSCs grown as neurospheres were dissociated with StemPro Accutase into single cell suspensions. 5 million cells were electroporated with 2  $\mu\text{g}$  of mCherry or Cre-T2A-mCherry plasmid using the Mouse Neural Stem Cell Nucleofector kit according to the manufacturer's protocol (Lonza VPG-1004) and plated in NSC maintenance medium. For each plasmid, 2 electroporations per culture were performed to produce enough mCherry+ cells for subsequent assays. The following day, mCherry+ cells were purified by FACS, replated at 50,000 cells/ml, cultured for 3 days and then used for analyses.

### **Cell Cycle Profile Analysis by Propidium Iodide (PI) Staining and Flow Cytometry**

$10^5$  dissociated NSCs were stained with PI and analyzed by St. Jude Children's Research Hospital Flow and Cell Sorting Shared Resource. Results were plotted using the Modfit software.

### **EU Incorporation Assay**

Passage-1 NSCs were plated in NSC maintenance medium on poly-L-Lysine and laminin coated coverslips and, on the following day, labeled with 1 mM of EU for 1 h. Cells were then fixed and EU signal detected using the Click-It RNA imaging kit (Thermo Fisher Scientific C10329). Unlabeled cells (negative control) were also subjected to EU detection and showed minimal background signal. Image acquisition was performed below saturation with the same laser settings for all the samples using a Zeiss LSM 780 confocal microscope and a 40x objective lens. DAPI signal was used to delimit the nucleus and mean nuclear EU signal intensities per pixel per nucleus were quantified using Imaris. For each condition (genotype and treatment), 3 cultures with 100 cells per culture were analyzed.

### **Inhibitor Treatments**

Passage-1 NSCs were plated at 50,000 cells/ml in 6-well plates in NSC maintenance medium containing inhibitors at indicated dosages for 24 h. For CDK4/6 inhibitor PD 0332991 treatment, dead cells were removed using the Dead Cell Removal Kit (Miltenyi Biotec 130-090-101) before plating. 3 control and 3 *Lats1/2* dKO cultures were treated for each condition.

### **Quantifications of Mitotic Defects, DNA Damage, and p53 Activation**

Passage-1 NSCs were plated in NSC maintenance medium at 50,000 cells/ml on poly-L-Lysine and laminin coated coverslips. The following day, immunostaining was performed as described above. To examine mitotic defects, cells were stained with phospho-Histone H3 Ser10 (pHH3) and  $\gamma$ -Tubulin antibodies and imaged with a Zeiss LSM 780 microscope at 63x with a 1.5 optical zoom. Chromosome distribution, morphology, and microtubule organization was used to determine mitotic phases. 3 cultures per genotype with 100 mitotic cells per culture were analyzed. To examine DNA damage and p53 activation, cells were stained with  $\gamma$ H2AX and p53 antibodies and imaged with a Zeiss LSM 780 microscope at 40x. DAPI signal was used to delimit the nucleus area and mean nuclear  $\gamma$ H2AX signal intensities per pixel per nucleus were quantified with Imaris. The presence of nuclear p53 signal was quantified manually. 3 cultures per condition (genotype and treatment) with 50 cells per culture were analyzed.

### **Protein Synthesis Assay**

Nascent protein synthesis was assessed using the surface sensing of translation (SUnSET) assay as described (Schmidt et al., 2009). Passage-1 NSCs were grown on poly-L-Lysine and laminin coated coverslips and incubated with 10  $\mu\text{g}/\text{ml}$  of puromycin for 10 min or with 25  $\mu\text{M}$  of cyclohexamide for 5 min and then with 10  $\mu\text{g}/\text{ml}$  of puromycin for 10 min. Cells were fixed and permeabilized as described above, and stained with a mouse anti-Puromycin antibody using a MOM kit (Vector Laboratories). Image acquisition was performed below saturation with the same camera settings for all the samples using an Olympus BX63 microscope and a 40x objective. Total Puromycin immunofluorescence signals per cell were measured using Imaris. For each condition (genotype and treatment), 3 cultures with 50 cells per culture were analyzed.

### **Live Imaging of NSCs**

E13.5 cortices were dissociated with StemPro Accutase and cells electroporated with a modified Fucci plasmid using the Mouse Neural Stem Cell Nucleofector kit (Lonza VPG-1004). The plasmid encodes a mAG (the monomeric version of Azami Green) fused to the Src myristoylation signal and, connected via a T2A peptide, a mKO2 [a fast-folding variant of mKO (monomeric version of Kusabira Orange)] fused to human Geminin<sup>1-110</sup> that accumulates in S/G2/M phases of a cell cycle. After electroporation, cells were resuspended in NSC maintenance medium and plated at 20,000 cells/ml in a  $\mu$ -Slide 2 Well (Ibidi 80286) coated with 50  $\mu\text{g}/\text{ml}$  of fibronectin (Thermo Fisher Scientific PHE0023) and covered with a DIC lid for  $\mu$ -Slides (Ibidi 80055). After an overnight incubation, mKO2+ (orange) cells were imaged for 14 h by time-lapse microscopy using a Nikon C2 confocal microscope with an environmental chamber at 37°C, 5% CO<sub>2</sub> using a 20x objective lens with 15-min imaging intervals. For each imaging session, cells derived from one control and one *Lats1/2* dKO embryos were imaged. 4 sessions, using cells derived from 4 different control and dKO embryos, were performed and a total of 191 control and 186 dKO cells recorded. Data were analyzed using the NIS-Elements software.

### **DNA Fiber Assay and Data Analysis**

This assay was performed as previously described (Nieminuszczy et al., 2016; Schwab and Niedzwiedz, 2011). Passage-1 NSCs were incubated with 25  $\mu\text{M}$  of IdU for 20 min followed with 250  $\mu\text{M}$  of CldU for 20 min in NSC maintenance medium at 37°C. Cells were then harvested by centrifugation and resuspended to  $5 \times 10^5$  cells/ml. 2  $\mu\text{l}$  of the cell suspension was air-dried on a glass slide for 3 min and lysed in 200 mM Tris-HCl (pH 7.5), 50 mM EDTA and 0.5% SDS solution for 2 min. Slides were tilted at a 15° angle to let the fibers spread, air-dried for 5 h, and treated with methanol/acetic acid (3:1) for 10 min and 2.5 M HCl for 80 min. IdU and CldU were detected using specific antibodies. DNA fibers were imaged using a Zeiss LSM 780 confocal microscope at 63x with a 2x optical zoom. For each genotype, 3 cultures were analyzed. From each culture, 100 to 125 fibers were imaged and measured. Fiber length

was measured with ImageJ. For the statistical analyses of sister-fork ratios and 2-segment ratios, since the data deviated from normal distribution (determined by Shapiro test for normality, both control and dKO groups were associated with  $P < 0.0001$ ), the tests for comparing the median and dispersion were computed by using non-parametric tests. The permutation-based Wilcoxon rank-sum test was used for median test and the permutation-based Ansari-Bradley test was used for dispersion test. These analyses were performed using R 3.4.2. Codes are available upon request.

### Affymetrix Microarray and Data Analysis

Total RNA was extracted from 3 control and 3 *Lats1/2* dKO E12.5 cortices using Trizol. 100 ng of total RNA from each sample was converted to biotin-labeled cDNA using the Affymetrix WT protocol, then hybridized to an Affymetrix Mouse Gene 2.0 ST GeneChip (Life Technologies). Signals from scanned arrays were normalized and summarized by the RMA algorithm using the Affymetrix Expression Console software v1.1. Differentially expressed transcripts were identified by ANOVA (Partek Genomics Suite v6.6) and the false discovery rate (FDR) estimated using the Benjamini-Hochberg method. Because none of the transcripts achieved  $FDR < 0.05$ , those with  $P \leq 0.05$  and  $\log_2$  fold change ( $\log_2FC$ )  $\geq 0.5$  or  $\leq -0.5$  were listed in [Table S1](#). Gene set enrichment analysis was performed using curated pathways obtained from MSigDB (Broad Institute) as previously described ([Subramanian et al., 2005](#)). Ranking of genes was calculated using the signal-to-noise algorithm, and a  $P$ -value for each gene set was estimated by comparing the observed enrichment score to that obtained from a null distribution computed from 1000 permutations of genes within gene sets. FDR was estimated as previously described ([Subramanian et al., 2005](#)).

### Cell Number Normalized (CNN) RNA-Seq and Data Analysis

Telencephalons from E12.5 embryos were dissected, dissociated with StemPro Accutase, and passed through a 40- $\mu$ m cell strainer to obtain single-cell suspensions. Cells were counted and  $1.0 \times 10^6$  cells were pelleted by centrifugation. Diluted ERCC spike-in mix (1:20, Thermo Fisher Scientific 4456740) was added to cell pellets and Trizol prior to RNA extraction at a ratio of 1  $\mu$ l of diluted ERCC spike-in mix per million cells. RNA was purified using a Direct-zol RNA kit (Zymo Research R2052) and eluted in 25  $\mu$ l of elution buffer.

Library preparation and sequencing were performed by the Genome Sequencing Facility at St. Jude Children's Research Hospital. RNA quality was checked by a 2100 Bioanalyzer RNA 6000 Nano assay (Agilent) before library generation. Libraries were prepared from 350 ng of total RNA using the TruSeq Stranded Total RNA Library Prep Kit (Illumina 20020597), then quantified using the Quant-iT PicoGreen dsDNA assay (Life Technologies). Samples were sequenced on Illumina HiSeq4000, obtaining 100 million 100-bp paired-end reads. RNAs from 5 control and 4 dKO embryos were sequenced.

Sequences were mapped to the mm9 genome with additional ERCC sequences using the STAR aligner ([Dobin et al., 2013](#)). Transcript level data was counted using HTSEQ ([Anders et al., 2015](#)). Raw counts were divided into transcript counts and ERCC counts. For quality control purposes, the linearity of the ERCC spike-in controls were considered and two spike-ins that consistently across all samples did not conform to the expected order (which is likely to be a manufacturer's error) were excluded from the ERCC raw counts. Transcript read counts and ERCC read counts were then used to determine normalization factors. Data were voom fitted and contrasted to determine differentially expressed genes using the empirical Bayes method in limma in R 3.4.0 ([Law et al., 2014](#)). Data visualizations were performed in STATA/MP 14.2 (StataCorp). Intron read counts were analyzed in the same manner. The splicing score of each transcript was calculated using the following equation:

$$\text{Splicing Score} = \frac{\text{Intronic reads per base}}{\text{Exonic reads per base}}$$

Bioinformatics analyses of differentially expressed genes were performed using Enrichr <http://amp.pharm.mssm.edu/Enrichr/> ([Chen et al., 2013](#); [Kuleshov et al., 2016](#)). Enrichment scores were displayed as combined scores, which is a combination of the  $P$ -value computed using the Fisher's exact test and the z-score computed by assessing the deviation from the expected rank, in the main text. Full lists with a FDR (adjusted  $P$  value) cutoff of 0.01 are provided in [Table S2](#).

### NanoString Analysis

Total RNA from 3 control and 3 *Lats1/2;Nestin-Cre* dKO E12.5 telencephalons, each sample containing  $1.0 \times 10^6$  dissociated cells, was extracted as described above. 7.5  $\mu$ l of total RNA was subjected to NanoString nCounter analysis. The mouse PanCancer Pathways Panel was chosen because it contained  $\sim 200$  genes that were found to be upregulated ( $\log_2FC > 0.5$ ) by CNN RNA-seq analysis. Raw counts were converted to  $\log_2$  values and used to calculate  $\log_2FC$  of dKO vs. control. Data were plotted either without further normalization (raw) or normalized to designated housekeeping genes in the panel.

### CNN qRT-PCR

Total RNA from 4 control and 4 *Lats1/2* dKO E12.5 telencephalons, each sample containing  $1.0 \times 10^6$  dissociated cells, was extracted as described above. 2  $\mu$ l of total RNA was used to generate 200  $\mu$ l of cDNA by using SuperScript III reverse transcriptase (Life Technologies). qPCR reactions were performed using 4.5  $\mu$ l of cDNA and iTaq Universal SYBR Green Supermix (Bio-Rad) on a CFX96 Real-Time System (Bio-Rad). Each reaction was performed in technical triplicates and averaged. Average values were then grouped based on genotype and the fold change between control and dKO calculated. PCR primers were designed using IDT's Realtime PCR

tool and tested using a serial dilution (1 to 1:1024) of cDNA generated from 1  $\mu$ g of total RNA. Primers were assessed based on linear amplification on a standard curve plot, amplification efficiency between 90–110%, and peak uniformity in a dissociation curve. Primers sequences are available upon request.

### Chromatin Immunoprecipitation and Sequencing (ChIP-Seq) and Data Analysis

Each E12.5 mouse brain was dissociated in 1 ml of cold PBS by pipetting. Protein–DNA complexes were crosslinked by incubating in 1% formaldehyde/PBS (Sigma F1635) for 10 min at RT with gentle rotation. Crosslinking was stopped with 125 mM glycine/PBS for 5 min and washed 3 times with cold PBS. Cells were lysed in 1 ml lysis buffer (50 mM HEPES-KOH [pH 7.5], 140 mM NaCl, 1 mM EDTA, 10% Glycerol, 0.5% NP-40, 0.25% Triton X-100) supplemented with protease and RNase inhibitors for 10 min at 4°C with gentle rotation. Nuclei were pelleted at 1800 rcf for 2 min, washed with 1 ml wash buffer (10 mM Tris-HCl [pH 8.0], 200 mM NaCl, 1 mM EDTA, 0.5 mM EGTA) supplemented with protease and RNase inhibitors for 10 min, and lysed in 900  $\mu$ l nuclear lysis buffer (10 mM Tris-HCl [pH 8.0], 100 mM NaCl, 1 mM EDTA, 0.5 mM EGTA, 0.1% Na-Deoxycholate, 0.5% N-Lauroylsarcosine) for 10 min. Lysed nuclei (300  $\mu$ l/1.5 ml sonication tube) were sonicated for 5 cycles of 15-sec on and 45-sec off in a Qsonica Q800R2 sonicator. Chromatin was quantitated and diluted with nuclear lysis buffer to  $\sim$ 500 ng/ $\mu$ l and further sonicated for 10 cycles of 15-sec on and 45-sec off to obtain an average DNA fragment size of  $\sim$ 300 bp. Sonicated chromatin was centrifuged at 14,000 rpm for 10 min and the supernatant chromatin was either used for ChIP or flash frozen and stored at  $-80^{\circ}$ C.

10% of chromatin from each ChIP reaction was used as the input control. For each ChIP reaction, 30  $\mu$ g of chromatin was incubated with 1.5  $\mu$ g of H3K4me3 antibody (Millipore 07-473) or normal rabbit IgG (Cell signaling #2729S) overnight at 4°C and with 25  $\mu$ l of Protein-A Dynabeads (Invitrogen) for 1 h. Beads were washed at RT with RIPA buffer (50 mM HEPES-KOH [pH 7.6], 500 mM LiCl, 1 mM EDTA, 1% NP-40, 0.7% Na-deoxycholate) 5 times and with TE buffer (10 mM Tris-HCl [pH 8.0], 0.1 mM EDTA) once. Chromatin was eluted by incubating in 300  $\mu$ l of elution buffer (50 mM Tris-HCl [pH 8.0], 10 mM EDTA, 1% SDS) for 5 min at RT with vortexing. After reverse-crosslinking at 65°C overnight with the addition of 18  $\mu$ l NaCl (5 M) and 2  $\mu$ l proteinase K (10 mg/ml), DNA was extracted using a PCR purification kit (QIAGEN #28106) and quantified using the Quant-iT PicoGreen dsDNA assay.

Sequencing libraries were prepared from 10 ng of DNA using the NEBNext ChIP-Seq Library Prep Reagent Set for Illumina with NEBNext Q5 Hot Start HiFi PCR Master Mix according to the manufacturer's instructions (New England Biolabs) with the following modifications: a second 1:1 Ampure cleanup was added after adaptor ligation and the Ampure size selection step prior to PCR eliminated. Completed libraries were analyzed for insert size distribution on a 2100 BioAnalyzer High Sensitivity kit (Agilent Technologies) or Caliper LabChip GX DNA High Sensitivity Reagent Kit (PerkinElmer). Libraries were quantified using the Quant-iT PicoGreen dsDNA assay (Life Technologies) and Kapa Library Quantification kit (Kapa Biosystems). Fifty-cycle single-end sequencing was performed on an Illumina HiSeq 2500 or HiSeq 4000.

ChIP-Seq reads were aligned to mm9 (MGSCv37) using the BWA software (version 0.7.12-r1039, default parameter). Duplicated reads were marked using the Picard software (version 2.6.0-SNAPSHOT) and only non-duplicated reads used for analysis using SAMtools (parameter “-q 1 -F 1024” version 1.2). Data quality control (QC) follows ENCODE criteria. Relative strand correlation (RSC) values were calculated and the fragment size estimated under the support of R (version 2.14.0) by SPP (version 1.1) with packages caTools (version 1.17) and bitops (version 1.0-6). At least 10 million unique reads with RSC > 1 was required to pass QC. 2 control and 2 *Lats1/2* dKO samples passed QC. Bigwig files were generated by extending each read to the best fragment size (the smallest fragment size estimated by SPP) and manually inspected using IGV genome browser for clear peaks and low background noise. MACS2 (version 2.1.1.20160309) was used to call peaks using the best fragment size with a cutoff of FDR < 0.05. Peak calling results for H3K4me3 ChIP were merged into two bed files, one for control and one for *Lats1/2* dKO (bedtools 2.23.0). Peak annotation was performed on the merged results with Homer version 4.5. Peaks within  $\pm$  5 kb of the transcription start site (TSS) were retained and de-duplicated by gene name and the membership compared between dKO peaks and control peaks (STATA/MP 14.2).

### QUANTIFICATION AND STATISTICAL ANALYSIS

Statistical analyses were performed using the GraphPad Prism 7 software unless otherwise noted in above sections. Statistical significance (*P* values) were calculated by unpaired two-tailed Student *t*-test unless otherwise noted. Statistical significance was denoted as follows: \**P* < 0.05; \*\**P* < 0.01; \*\*\**P* < 0.001; n.s., not significant. Area-proportional Venn diagrams were generated by using the eulerAPE software <http://www.eulerdiagrams.org/eulerAPE/>.

### DATA AND SOFTWARE AVAILABILITY

Microarray, RNA-seq, and ChIP-seq data associated with this manuscript can be found at the GEO repository under accession number GEO: GSE120016.